Topics in Catalysis (2024) 67:344–362
https://doi.org/10.1007/s11244-023-01850-3

ORIGINAL PAPER

High Surface Area Assemblies of Gold Nanoparticles on Hydrophilic Carbon Fiber Paper with Ionomer Overlayers for Aqueous CO_2 Reduction Electrocatalysis to Clean Syngas

Ryland C. Forsythe[1] · Connor P. Cox[2] · Madeleine K. Wilsey[2] · Wanqing Yu[1] · Astrid M. Müller[1,2,3]

Accepted: 15 July 2023 / Published online: 11 August 2023

Abstract
We report a universal approach for the utilization of nanoparticles on inexpensive, high surface area carbon substrates in aqueous applications. We immobilized gold nanoparticles from aqueous colloid on hydrophilic carbon fiber paper and assessed this electrode assembly in aqueous carbon dioxide reduction electrocatalysis. Uniform distributions of gold nanoparticles on carbon fibers and stable electrocatalytic current generation indicated that immobilization of gold nanoparticles on hydrophilic carbon fiber paper was successful. Surface analysis before and after electroreduction revealed that the detachment of citrate capping ligands enhanced the amount of exposed surface gold and concomitantly increased the CO-to-H_2 ratio in subsequent CO_2 reduction electrocatalysis. Systematic variations of ionomer overlayers controlled the ratio of produced CO and H_2 towards useful syngas compositions and revealed mechanistic insights into catalyst microenvironments, to enhance CO selectivity. Our results demonstrate that hydrophilic carbon fiber paper is an excellent high surface area electrode substrate for the utilization of nanoparticulate electrocatalysts in aqueous electrolyte.

Keywords Electrocatalysis · Nanocatalyst · Carbon dioxide reduction · Carbon fiber paper · Syngas · Ionomer overlayers · Selectivity · Nafion · Sustainion · Microenvironment

1 Introduction

A low-carbon economy demands that we generate fuels and chemicals that do not contribute to climate change [1, 2]. Electrocatalytic conversion of carbon dioxide and water into liquid fuels and useful chemicals with only solar electricity as energy input is carbon-neutral by recycling and thus diminishes net CO_2 emissions [3–5]. To enable this decarbonization, we must develop new catalysts and electrode supports, to effectively mediate the chemical processes that produce upgraded products [2].

Gold cathodes catalyze CO_2 reduction to produce CO, H_2, and minor amounts of formate [6–8]. Mixtures of H_2 and CO are the principal components of synthesis gas (syngas), which is a key intermediate for the production of hydrogen, ammonia, and methanol, as well as a precursor in Fischer–Tropsch synthesis and other thermochemical catalysis to industrially produce hydrocarbons and oxygenates, such as fuels, light olefins, ethylene, and aromatics [9–11]. Currently, syngas is made by steam reforming of natural gas or naphtha, or coal gasification, which generally produces syngas composed of 30 to 60% carbon monoxide, 25 to 30% hydrogen, 5 to 15% carbon dioxide, 0 to 5% methane, some water vapor, and smaller amounts of hydrogen sulfide, carbonyl sulfide, ammonia, and other trace contaminants [12]. Syngas obtained from fossil feedstocks commonly has to be purified for downstream catalytic processes. In contrast, syngas derived from electrocatalytic CO_2 reduction is clean because its gaseous products consist only of H_2 and CO, eliminating the need for purification.

Ryland C. Forsythe and Connor P. Cox contributed equally to this work.

✉ Astrid M. Müller
astrid.mueller@rochester.edu

[1] Department of Chemical Engineering, University of Rochester, 14627 Rochester, NY, USA

[2] Materials Science Program, University of Rochester, 14627 Rochester, NY, USA

[3] Department of Chemistry, University of Rochester, 14627 Rochester, NY, USA

Nanomaterials are often better catalysts than bulk solids because of maximized surface area; additional activity benefits may arise from metastability at the nanoscale and nano- and atomic-scale control of nanostructures [1]. For use in electocatalysis, nanoparticles must be immobilized on electrically conducting, inert electrode supports to provide electrical contact to the catalytic nanoparticles, without corrosion of the support material. Electrode support materials that possess high surface area, such as carbon fiber paper (CFP), additionally enhance performance (Fig. 1).

Carbon is commonly used as supporting electrode material, in the form of glassy carbon, highly oriented pyrolytic graphite, carbon nanotubes, carbon fibers, carbon cloth, or graphene. Its availability, low cost, and robust nature make it economically desirable, compared to metal electrodes [13]. Additionally, carbon is chemically inert and electrically conductive; it also has a wide potential window in both aqueous and non-aqueous electrolytes, which makes carbon compatible with many electrochemical applications [14, 15]. Specifically for CO_2 reduction, electrode supports made of carbon have the advantage that carbon has a high overpotential for hydrogen evolution, thus suppressing this competing reaction [13].

So far, nanoparticulate catalysts for aqueous CO_2 reduction have not been assessed on hydrophilic CFP supports. Reported nanoparticulate CO_2 reduction catalysts are the following: copper is the most well studied cathode material for CO_2 reduction electrocatalysis; copper nanoparticles have been examined on metallic copper, glassy carbon, carbon paper, carbon nanotubes, neat or nitrogen-doped graphene or graphene oxide, neat or nitrogen-doped nanodiamond on Si, or polytetrafluoroethylene supports [16, 17]. A copper-gold nanowire array was tested on gold foil [16, 17]. Copper-free nanocatalysts on various supports have also been reported for aqueous electrocatalytic CO_2 reduction [18–21], albeit most of them without or with only limited physical analysis of the nanomaterial–support assembly. Further, in the case of hydrophobic supports it remains unclear how aqueous electrolytes were able to wet these supports to minimize resistance in liquid electrochemical cells; hydrophilicity is needed to take advantage of large internal surface areas of porous carbon supports. Nanocatalysts comprised of FeOOH, Fe–N–C, Ni, Ni-doped nitrogenated carbon, Pd, Ag_2O, CdS, Sn loaded on nitrogenated carbon, Au mixed with carbon black, or Au embedded with graphene have been investigated on hydrophobic carbon paper, which in several instances was Teflon-coated. Nitrogen-doped carbon nanoparticles, Ni–Fe nanoalloy on N-doped carbon, an aerogel composite of Sn on carbon, or SnO_2 nanosheets catalyzed CO_2 electroreductions on as-purchased, unspecified

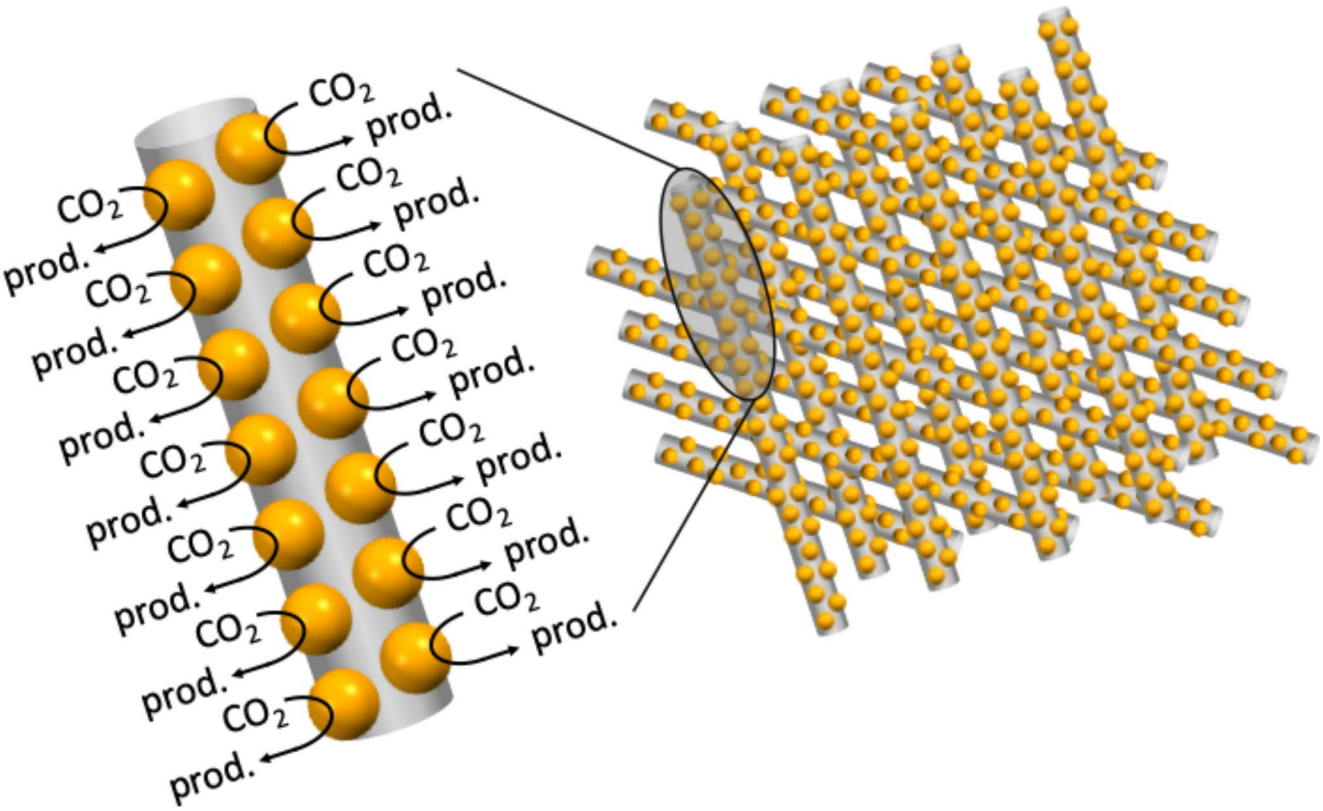

Fig. 1 Schematic of nanoparticulate catalysts (yellow) on carbon fibers (gray), illustrating how the high surface area of a nanoparticle–CFP assembly enhances the generation of CO_2 reduction electrocatalysis products (prod.)

carbon cloth. Nanomaterials consisting of N- or F-doped carbon, Ni, MoS_2, Pd, Ag, SnO_2, Au, or Bi on glassy carbon served as cathodes in CO_2 reduction electrocatalysis. Indium nanocrystals on graphite and Au nanoparticles on graphene foam have been studied for CO_2 reduction. Carbon nanotubes and nanofibers, either neat, doped with nitrogen or sulfur, or loaded with SnO_x or Au nanoparticles, catalyzed CO_2 electroreductions. Nitrogen-doped carbon, RuO_2, Ag, SnO_2, Au, or Bi nanomaterials on metal foils or thin film supports have also been reported [18–21].

Economical CFP supports enable greatly enhanced catalyst mass activities [22] and ergo significant cost savings particularly for nanocatalysts made of precious metals, such as gold. As-purchased CFP is hydrophobic, which prevents widespread use in aqueous applications. Several challenges exist for the utilization of nanoparticles on CFP supports in aqueous electrolytes: (i) CFP must be rendered hydrophilic without altering carbon fiber mesostructures for mass transport and mechanical stability reasons, (ii) nanoparticles must be distributed uniformly on the carbon fibers of hydrophilic CFP, and (iii) nanoparticles must be immobilized on hydrophilic CFP such that they do not detach during electrocatalysis. Our work offers solutions to all three challenges.

Carbon surfaces must be hydrophilic in liquid aqueous applications, including in electrocatalysis mediated by nanoparticles [15, 23–33]. We recently reported a green-chemistry process that imparted long-lasting hydrophilicity to initially hydrophobic CFP by selective carbon surface hydroxylation [22, 34]. Our universal approach solved a long-standing challenge in nanoparticle electrocatalysis in aqueous media, by providing hydrophilic, high surface area carbon scaffolds that enable electrical contact to individual nanoparticles.

In addition to utilization in liquid aqueous applications, hydrophilic CFP [22] enables the deposition of nanoparticles from aqueous colloids, such as the gold colloid of this work, because the water that surrounds the nanoparticles can completely penetrate into the three-dimensional network of the carbon fibers, thus taking full advantage of the high internal surface area of CFP architectures for nanoparticle immobilization. Such nanoparticle–CFP assemblies have many applications, including serving as electrodes in aqueous electrocatalysis, toward the development of climate-friendly successor technologies for sustainable energy [3, 16, 35–46]. Here, we demonstrate the successful implementation of gold nanoparticles with CFP electrode supports for CO_2 reduction electrocatalysis in aqueous electrolyte to clean syngas, whose CO-to-H_2 ratio was controlled by the applied potential or ionomer overlayers.

Ionomers are copolymers of nonionic and ionic polymer units and are often used in ion selective membranes due to their ability to conduct ions of opposite charge to the ionic polymer units. Ionomer overlayers serve three purposes: (i) improved adhesion of nanocatalysts to supporting electrode surfaces, (ii) increased charge transport from the nanoparticles to the electrode, and (iii) enhanced transport of liquid and gas phase species within the boundary layer of the electrode. The most commonly used and well investigated ionomer is Nafion, which forms lamellar structures of hydrophilic and hydrophobic channels comprised of sulfonate and difluoromethylene groups, respectively [47]. The hydrophilic channels transport electrolyte and liquid phase species to and from the catalyst surface, while the hydrophobic channels facilitate gas transport [48]. Sustainion is a popular ionomer in the CO_2 reduction field because of a 20-fold enhanced solubility for CO_2 compared to water [49]. Sustainion is an N-methylimidazolium-functionalized styrene polymer with high hydroxide ion conductivity and stability in pH ranges of 2–13 [50]. While ionomers have been used in CO_2 reduction electrocatalysis to improve cathode stability and enhance product selectivity [48, 49, 51–60], a systematic study of different ionomers on gold nanoparticles immobilized on CFP has not been conducted so far.

Carbon dioxide reduction electrocatalysis requires protons to proceed, making hydrogen evolution an inevitable, yet unwanted, competing reaction [3]. Strategies to suppress hydrogen evolution center on catalyst design, process optimization, and engineering of the microenvironment at the catalyst surface. Key design criteria of the catalyst microenvironment for CO_2 reduction to useful carbon products are (i) eliminate water at the catalyst surface to suppress H_2 evolution (albeit water is needed near the catalyst in aqueous CO_2 reduction), (ii) enhance the mass transport of CO_2 molecules to the catalyst surface, and (iii) facilitate the binding and bending of CO_2 at the cathodic catalyst surface upon the first electron transfer, to form the surface-bound C–O intermediate. Here, we report a systematic study on aqueous CO_2 reduction catalyzed by gold nanoparticles immobilized on hydrophilic CFP with engineered microenvironments at the catalyst surface.

2 Methods

All chemicals were used as received. Deionized water was obtained from a Thermo Scientific Barnstead Smart2Pure Pro UV/UF 15 LPH Water Purification System and had a resistivity of $\geq$17.5 MΩ • cm. All experiments were performed at room temperature. Data analysis and graphing were performed with Igor Pro 8.04 (Wavemetrics).

Carbon Fiber Paper (CFP) Treatment The acid-free process that imparts long-lasting hydrophilicity to CFP without

damaging the carbon fibers and their network architectures is described elsewhere [22, 34]. Briefly, we selectively functionalized CFP surfaces with hydroxyl groups by sonication of CFP in 1 M aqueous sodium dodecyl sulfate (SDS) solution, followed by electrooxidation in 0.1 M pH 8.7 aqueous $KHCO_3$ electrolyte at +1.63 V vs. Ag/AgCl for 20 min [22, 34]. Henceforward, this treatment is called SDS–electrooxidation.

Preparation of Cathodes from High-Surface-Area CFP Working electrodes were SDS–electrooxidation treated 2.4 cm wide × 3.8 cm high CFP pieces that were used neat or with immobilized gold nanoparticles (nanoComposix, 20 nm gold nanospheres, 0.05 mg mL^{-1} in 2 mM aqueous sodium citrate); 5.8 cm^2 geometric surface area was exposed to the electrolyte in the electrochemical H-cell. We immobilized 20 nm gold nanoparticles on hydrophilic CFP [22] (henceforward called AuNP–CFP assembly) by placing the CFP on the bottom of a custom-made Teflon tub, which was filled with 2 mL of gold nanoparticle colloid such that all CFP was uniformly covered. This Teflon tub was placed under a heat lamp at approximately 60 °C for 20 min. The resulting gold loading was 10 μg cm^{-2}_{geo}.

Removal of Citrate from AuNP–CFP Assemblies Citrate was removed from AuNP–CFP assemblies by electroreduction in 0.1 M pH 8.7 aqueous $KHCO_3$ electrolyte at −1.28 V vs. Ag/AgCl for 30 min, with CFP as the counter electrode. Subsequently, AuNP–CFP assemblies were rinsed well with deionized water and dried in a clean nitrogen stream. Electroreductive citrate removal was carried out in a separate electrochemical cell, to minimize the presence of citrate during CO_2 reduction experiments.

Preparation of Overlayers on AuNP–CFP Assemblies ssemblies served as working electrNafion overlayers with 0.1 mg cm^{-2}_{geo} ionomer loading were prepared by adding 18.44 μL of 5 wt% Nafion 117 containing solution (Sigma Aldrich) to 981.56 μL of 2-propanol (Fisher Chemical, ACS grade) before drop casting the ionomer suspension onto an AuNP–CFP electrode that had been subjected to citrate removal; the AuNP–CFP electrode with the ionomer suspension was placed in the Teflon tub and dried under a heat lamp at 60 °C for 25 min. Potassium-exchanged Nafion solutions were prepared by modification of a reported procedure for alkali ion exchange [61]. A solution with a 2/1 (v/v) ratio of Nafion 117 solution and 0.1 M or 0.4 M aqueous KOH (Thermo Scientific, 99.98%) was sonicated for 5 min, after which the solution sat in a covered vial at room temperature for 24 h, to obtain 0.1 or 0.4 M K^+-exchanged Nafion solutions, respectively. Likewise, a solution with a 2/1 (v/v) ratio of Nafion 117 solution and 0.1, 0.4, 0.8, or 1.5 M CsOH (Acros Organics, 99.95%) was sonicated for 5 min, after which the solution sat in a covered vial at room temperature for 24 h, to obtain 0.1, 0.4, 0.8, or 1.5 M Cs^+-exchanged Nafion solutions, respectively. Potassium- or cesium-exchanged Nafion overlayers on AuNP–CFP assemblies with 0.1 mg cm^{-2}_{geo} ionomer loading on were prepared by adding 27.66 μL of 0.1 or 0.4 M K^+-exchanged or 0.1, 0.4, 0.8, or 1.5 M Cs^+-exchanged Nafion solution to 972.34 μL of isopropanol, mixing the resulting solution with a pipette tip, and drop casting 1 mL of the solution on an AuNP–CFP electrode that had been subjected to citrate removal; the AuNP–CFP electrode with the ionomer suspension was placed in the Teflon tub and dried under a heat lamp at 60 °C for 25 min. Sustainion overlayers with 0.1 mg cm^{-2}_{geo} ionomer loading were prepared by adding 18.44 μL of 5 wt% Sustainion solution (Dioxide Materials) to 981.56 μL of ethanol (Pharmco, ACS grade); as purchased Sustainion was suspended in ethanol, which is why ethanol was used as the dispersant. The resulting Sustainion solution was mixed with a pipette tip, and 1 mL of the solution was drop-cast on an AuNP–CFP electrode that had been subjected to citrate removal; the AuNP–CFP electrode with the ionomer suspension was placed in the Teflon tub and dried under a heat lamp at 60 °C for 25 min.

Physical Characterization High-resolution scanning electron microscopy (SEM) images were collected at UR-Nano, using 12,000× or 100,000× magnification at a Zeiss Auriga scanning electron microscope, equipped with a Schottky field emission emitter, and operated at 1.00 kV with a working distance of 4.9 mm; images were collected in secondary electron mode to enhance elemental contrast. Electron-dispersive spectroscopy (EDS) data were taken with an EDAX Octane Elect Plus system in conjunction with EDAX APEX software, to obtain EDS spectra and elemental maps of gold and carbon. The SEM image of Fig. 2C was acquired in backscatter mode to enhance elemental contrast, using a JEOL JSM-5900LV SEM instrument, equipped with a thermionic tungsten electron gun, operated at 25 kV with a working distance of 10 mm. CFP samples were immobilized on 1-inch diameter aluminum SEM stubs (Ted Pella) with carbon tape (Electron Microscopy Sciences).

X-ray photoelectron spectra (XPS) were obtained with a Kratos Axis Ultra XPS instrument, which was equipped with a monochromatized Al Kα radiation source, operated in high-power mode at 200 W and 15 kV, with a base chamber pressure of 3.0×10^{-8} mbar. Samples were immobilized on double-sided adhesive copper tape. Survey scans were obtained between 0 and 1200 eV with a step size of 1 eV, a dwell time of 200 ms, and an analyzer pass energy of 140 eV averaged over 5 scans. Core level region scans for

C 1s, O 1s, and Au 4f were acquired at the corresponding binding energy ranges with a step size of 0.1 eV, an average dwell time of 260 ms, and an analyzer pass energy of 20 eV averaged over 5 scans. Binding energies were referenced to the C 1s peak arising from adventitious carbon, taken to have a binding energy of 284.8 eV [62]. Binding energies and quantitative peak areas were derived after Shirley background subtraction [63] and Gaussian/Lorentzian envelope peak fitting. For the quantification of different components, instrument-specific atomic sensitivity factors determined from standard materials were used. XPS analysis was performed with CasaXPS (Version 2.3.24).

Electrocatalysis We used a custom-made polycarbonate electrolysis cell provided by the Jaramillo group (Stanford University) for electrochemistry experiments [64]. In this cell, the working and counter electrode compartments each had electrolyte volumes of 9 mL and gas headspaces of approximately 2 mL. Both compartments of the electrochemical cell were filled with CO_2-saturated 0.1 M pH 6.8 aqueous $KHCO_3$ buffer, and the cell was continuously sparged with humidified CO_2 (Airgas, 99.99%) at room temperature for 20 min to ensure that the electrolyte remained saturated with CO_2 prior to electrochemical data collection. Throughout electrocatalysis, calibrated mass flow controllers (Aalborg) maintained the flow of CO_2 at 20 mL min^{-1} through the cell. Gas diffusion frits (Wilmad Labglass) were used to enhance CO_2 saturation in the electrolyte. The working and counter electrodes each had 5.8 cm^2 geometric surface area and were separated by a Selemion anion exchange membrane (AMV-N), which was stored overnight in 0.1 M aqueous $KHCO_3$. The counter electrode was a Pt foil (Aldrich, 0.025 mm thick, 99.9%) and the reference electrode was an Ag/AgCl electrode. Supremium aluminum foil (Ultra-Clean) was used to electrically contact the working and counter electrodes to the leads of the potentiostat (BioLogic, SP-150-EIS). Solution resistances were determined from impedance measurements and compensated using automatic 85% iR compensation; the remaining 15% was corrected manually after data collection, following a published procedure [64]. Solution resistance measurements were conducted using the ZIR function of the BioLogic potentiostat. In accordance with a published procedure developed for our specific cell geometry [64], we used a frequency of 10 kHz for solution resistance measurements. Each electrochemical experiment started with a measurement of solution resistance, followed by the collection of two cyclic voltammograms from +2.3 V to −1.2 V vs. the reversible hydrogen electrode (RHE) at a scan rate of 50 mV s^{-1} (Figure S1), taking chronoamperometry data at −0.68 V vs. RHE for 2 h, and concluding with the collection of two more cyclic voltammograms under virtually the same conditions as the initial ones. Carbon dioxide reduction products were detected by an in-line gas chromatograph (GC, SRI Instruments, Multi-Gas #5 configuration) that was connected to the headspace of the working electrode compartment of the electrochemical cell. Hydrogen was measured by a thermal conductivity detector, while CO and other hydrocarbon products were identified by a flame ionization detector equipped with a methanizer. Following a published procedure [64], we programmed the gas chromatograph to measure produced gases every 20 min, starting 5 min after the start of the chronoamperometry experiment. A certified standard calibration gas (Airgas) was used to calibrate the gas chromatograph and obtain molar concentrations of produced gases by quantifying peak areas. Faradaic efficiencies (*FE*) were calculated from these molar concentrations in combination with the average charge transferred during the gas chromatograph sampling, using the following equation:

$$FE(\%) = \frac{N_{\text{product}}}{N_{\text{total}}} = \frac{c_{product}(\text{PPM}) \cdot n_e \cdot 1.327\left(\frac{C}{8}\right)}{|I_{average}|(A)}$$

In this equation, N_{product} is the number of electrons transferred to make gas-phase product, N_{total} is the total number of electrons transferred, c_{product} is the molar concentration of gaseous product in units of ppm, n_e is the number of electrons required to reduce one molecule of CO_2 to one molecule of product, and I_{average} is average current during gas chromatography sampling in units of A. The constant parameters in the equation led to the number 1.327 in units of C s^{-1}; this number was derived from multiplying the number of moles sampled (4.126×10^{-5} mol) with Avogadro's number and the elementary charge, and then dividing by the time it took to fill the sample loop of the gas chromatograph (3 s). Average faradaic efficiencies were calculated by averaging data points from 25 min forward, to exclude artifacts from solid-state material reductions. Error bars of faradaic efficiencies are the standard deviations of the total faradaic efficiencies. Likewise, error bars of partial current densities are the standard deviations of the total partial current densities.

Quantification of Formate by NMR ^{1}H NMR spectra were recorded at 500 MHz on a Bruker DPX-500 spectrometer at room temperature. A water pre-saturation method adjusted to the intensity of water signal, considering 10% D_2O and 90% H_2O proportion was applied, after which a 90° width pulse was applied, followed by FID acquisition. Spectral width was 13.015 ppm large (6510 Hz) and centered on 4.826 ppm, with 32 kpt collected over 64 scans. Acquisition time was 2.5167 s. Spectra were phase corrected, an automatic baseline correction was applied, and manual bias and slope corrections were applied such that the integrals were flat on either side of the peak. Zero filling was applied by

doubling the size of the FID before the Fourier transform. Samples were prepared by adding 35 µL of D_2O with 35 mM DMSO and 50 mM phenol to 700 µL of electrolyte. Calibration curves for formate quantification were prepared using 6 samples ranging from 50 mM to 1.6 µM. Peak integrals were normalized with the DMSO peak area, equaling 100.

3 Results and Discussion

3.1 Assemblies of Gold Nanoparticles on Hydrophilic CFP

We prepared assemblies of CFP and gold nanoparticles as high surface area cathodes in aqueous CO_2 reduction electrocatalysis. We immobilized 20 nm gold nanoparticles on CFP (henceforward abbreviated AuNP–CFP) by soaking hydrophilic CFP [22] electrodes in aqueous citrate-capped gold colloid and drying under a heat lamp, resulting in a gold loading of 10 µg cm^2_{geo}. Untreated, hydrophobic CFP did not permit penetration of the aqueous gold colloid into the carbon fiber network. In fact, aqueous gold colloid droplets sat on top of the CFP surface, thus preventing nanoparticle deposition throughout the high internal surface area of CFP (Fig. 2A); the back side of hydrophobic CFP stayed completely dry. In contrast, hydrophilic CFP [22] was fully wetted by the aqueous gold colloid (Fig. 2B). Interestingly, the aqueous gold nanoparticle colloid did not wet the electrode tab of treated CFP (Fig. 2B); the tab remained hydrophobic because it was deliberately not immersed in the treatment solutions to keep it dry for electric contact without corrosion of the metal clamp at the lead to the potentiostat. Gold nanoparticles were uniformly distributed on carbon fibers, even deep within the carbon fiber network, as evidenced by SEM imaging (Fig. 2C, D, E); corresponding EDS maps and spectra are in Figures S2 and S3. The EDS data showed the presence of the elements carbon (from CFP and citrate), gold (from gold nanoparticles), and sodium (from sodium citrate). Our electrochemical cell required a working electrode of 2.3 cm × 3.9 cm size. This large geometric area impeded the use of a dispersant [65] or spin-coating to spread aqueous nanoparticle suspensions on hydrophobic surfaces. Besides, such approaches are not amenable to large-scale applications in commercially viable electrolyzers.

Electroreductive citrate removal from AuNP–CFP assemblies. We employed electroreduction in 0.1 M pH 8.7 aqueous $KHCO_3$ electrolyte at −1.28 V vs. Ag/AgCl to remove citrate from the AuNP–CFP assemblies, which were prepared from aqueous citrate-capped gold colloid. X-ray photoelectron spectroscopy (XPS) data of AuNP–CFP assemblies that were collected before and after this citrate-removal electroreduction revealed that more surface gold, relative to carbon, was detectable after citrate removal (Fig. 3). We obtained a more than 2.5-fold higher surface gold-to-carbon ratio of 0.065:1 after citrate-removal electroreduction than before (0.024:1); carbon from CFP and citrate contributed to the C 1s signal. Likewise, the surface gold-to-oxygen ratio increased more than six-fold from 0.16:1 to 1.05:1 upon electroreduction. The oxygen and carbon content of citrate, $C_6H_5O_7^{3-}$, as well as that

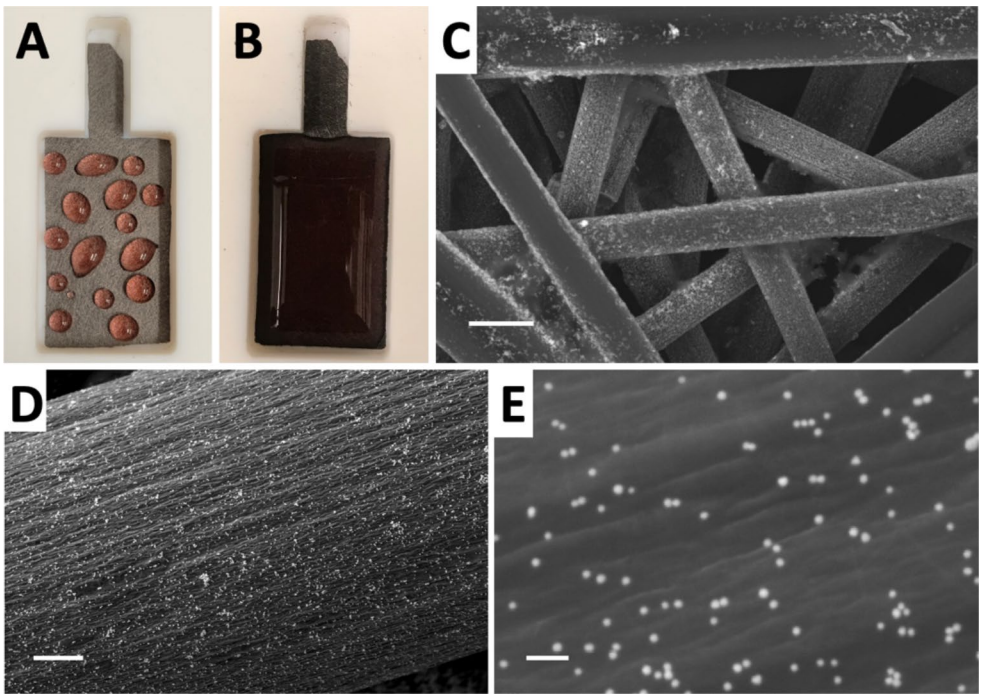

Fig. 2 Photographs of aqueous gold nanoparticle colloid on CFP that was horizontally placed in a Teflon tub; CFP was as-purchased and hydrophobic (A) or made hydrophilic by our green-chemistry treatment [22] (B). The hydrophobic electrode tab of treated CFP in (B) was not wetted by the aqueous gold colloid. SEM image of AuNP–CFP assembly, taken in backscatter mode to enhance the contrast between gold (bright) and carbon (dark), with a scalebar of 10 µm (C). High-resolution SEM images of AuNP–CFP assembly, taken in secondary electron mode to enhance the contrast between gold (bright) and carbon (dark), with scalebars of 1 µm (D) or 100 nm (E)

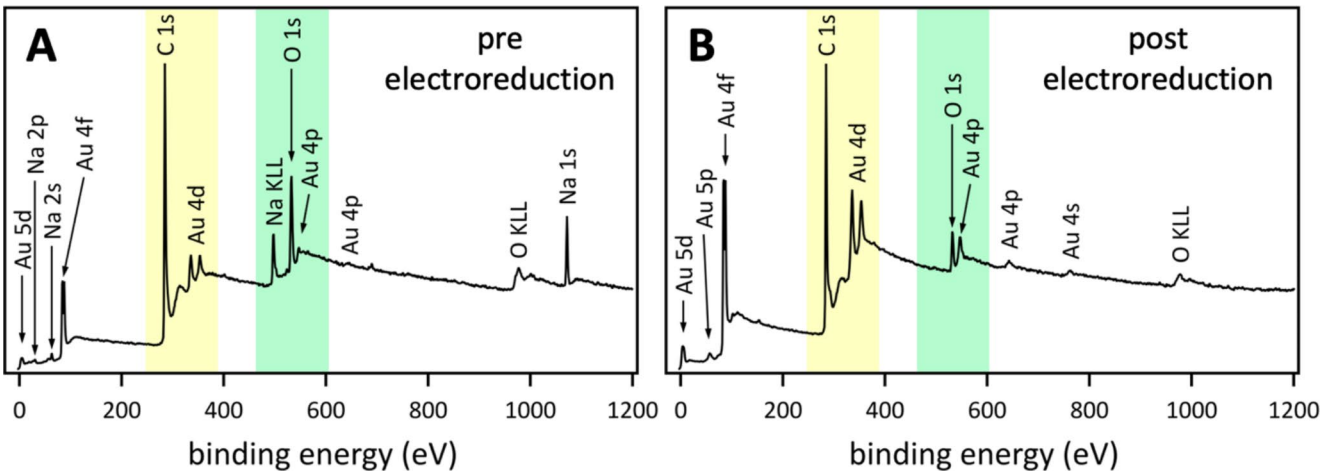

Fig. 3 Survey XPS data of AuNP–CFP assemblies, collected before (A) and after citrate-removal electroreduction (B). Highlighted in yellow are the C 1s and Au 4d core level regions, which show the surface gold-to-carbon ratio; highlighted in green are the O 1s and Au 4p core level regions, which visualize the surface gold-to-oxygen ratio

of hydrophilic CFP [22] comprised the O 1s and C 1s signals. Sodium was detected in pre-electroreduction XPS data because the gold nanoparticles we used were capped by sodium citrate to stabilize the aqueous colloid. No surface sodium was detectable post electroreduction, indicating detachment of capping ligands during electroreduction, consistent with our observation of higher Au:C and Au:O ratios after electroreduction, which provided evidence for the presence of uncapped surface gold.

High-resolution XP spectra in the Au 4f and O 1s core level regions showed significant changes of surface characteristics between AuNP–CFP assemblies before and after citrate-removal electroreduction (Fig. 4). We fitted the data with several peaks to identify individual surface species, in accordance with reported values. A detailed description of O 1s core level region peak fitting of hydrophilic CFP can be found elsewhere [22]. High resolution O 1s core level spectra required three peaks to match the measured data. One peak had a central binding energy range of 531.6 to 532.3 eV, attributable to C = O functional groups, whereas another peak exhibited a central binding energy range of 533.0 to 533.7 eV, attributable to C–O species [66–69]. Each citrate molecule contains four C–O and two C = O groups, which contributed to the measured O 1s signals. The O 1s C–O to C = O peak area ratio was 0.67:1 before citrate-removal electroreduction, and 0.37:1 after electroreduction, when surface citrate was detached. In both O 1s spectra, taken before and after electroreduction, we had to include a third peak to match the data. In the data collected before electroreduction (Fig. 4A), this peak possessed a higher binding energy than the C–O and C = O peaks. It had a central binding energy ranging from 535.3 to 536.0 eV and was attributable to adsorbed water [70, 71], which likely originated from the aqueous colloid we used for gold nanoparticle immobilization. Interestingly, no adsorbed water was present in XPS data that were taken after citrate-removal electroreduction, indicating surface water loss at the cathode upon loss of citrate capping ligands. In contrast, in the post-electroreduction O 1s data (Fig. 4B), the third peak was located at a lower binding energy than that of the C–O and C = O peaks. Its central binding energy ranged from 530.0 to 531.0 eV, attributable to Au_2O_3, in agreement with reported values [72–74]. Surface gold oxide likely resulted from oxidation of bare gold nanoparticles upon contact with ambient air after removal of the AuNP–CFP assembly from the electrochemical cell, washing with water, and drying before XPS data acquisition. We hypothesize that this native oxide layer is absent under cathodic polarization, during which metallic gold catalyzed the CO_2 reduction process. This hypothesis is corroborated by the fact that we did not observe a gold oxide peak in the pre-electroreduction O 1s data, as surface gold was capped by citrate, which did not leave bare gold exposed and thus inhibited the formation of Au_2O_3 in ambient air.

High resolution Au 4f core level spectra required four peaks to match the measured data (Fig. 4C, D, E, F). We observed two sets of peaks for the two spin-orbit split components Au $4f_{7/2}$ and Au $4f_{5/2}$. We constrained the intensity ratio of the Au $4f_{7/2}$ and Au $4f_{5/2}$ peaks to 4:3 to match the natural population of the spin states [74–76]. We obtained an Au 4f spin-orbit splitting of (3.7 ± 0.02) eV, in agreement with reported values for atomic Au [75–78]. We constrained the full-width-at-half-maximum values for all peaks in the Au 4f region to a range of 0.5–1.5 eV, in keeping with literature values [78–81]. In spectra collected before and after citrate-removal electroreduction, we predominantly observed metallic gold at the surface, with central binding energy ranging from 84.3 to 84.4 eV for Au $4f_{7/2}$ and 88.0

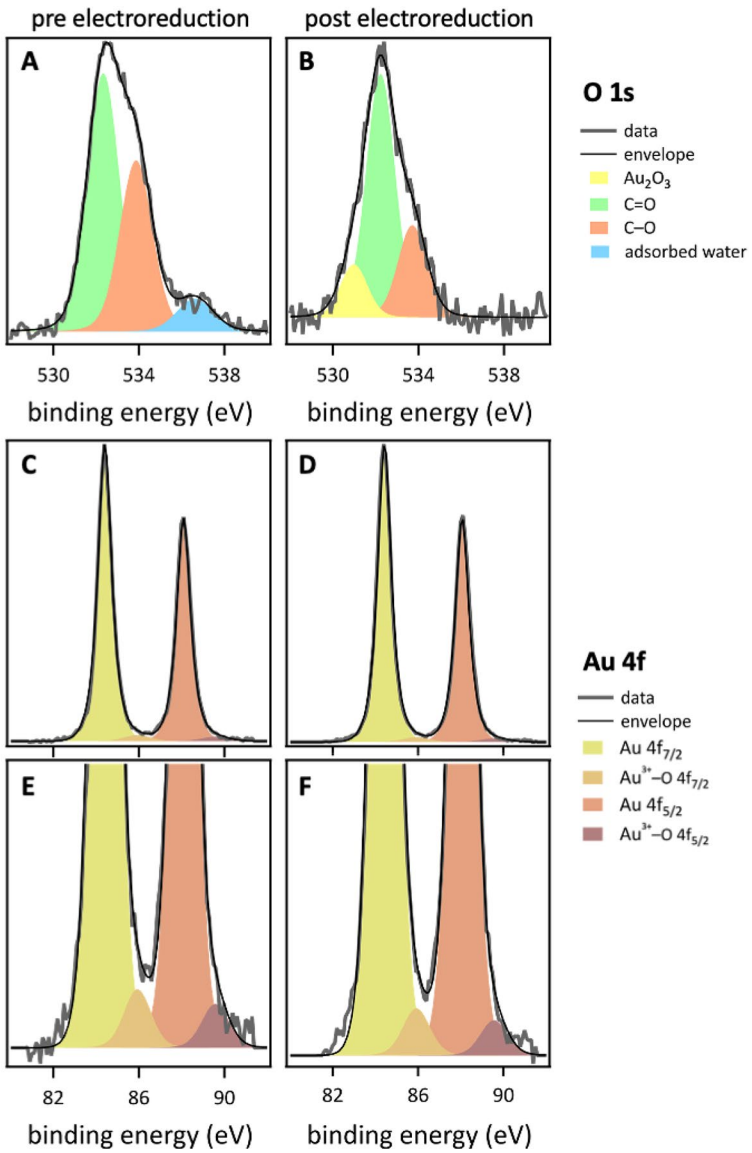

Fig. 4 High-resolution XPS data of AuNP–CFP assemblies in the O 1s (A, B) and Au 4f core level regions with *y*-axes that display the entire spectra (C, D) and with *y*-axes that were magnified by a factor of 10 (E, F), collected before (A, C, E) or after citrate-removal electroreduction (B, D, F)

to 88.1 eV for Au $4f_{5/2}$, in agreement with published values [72, 78, 82–84]. The minor species in both spectra had central binding energies ranging from 85.8 to 86.0 eV for Au $4f_{7/2}$ and 89.5 to 89.7 eV for Au $4f_{5/2}$, attributable to Au^{3+}–O [72, 74]. We observed a factor of 1.3 more surface Au^{3+}–O relative to metallic gold in XPS data taken before citrate-removal electroreduction than in those collected after electroreduction. Together with our analysis of the O 1s data, we conclude that surface Au^{3+}–O of AuNP–CFP assemblies before citrate-removal electroreduction originated from citrate ligands bound to trivalent gold. In contrast, surface Au^{3+}–O after electroreduction was due to native oxide formation in ambient air, which is corroborated by our observation of Au_2O_3 in the O 1s data. Overall, the XPS data of AuNP–CFP assemblies before and after citrate-removal electroreduction showed that our electroreduction enhanced the amount of bare gold at the surface and concomitantly eliminated adsorbed water upon detachment of hydrophilic sodium citrate capping ligands.

We collected high resolution XPS data in the K 2s core level region to exclude the presence of surface residues from the aqueous potassium bicarbonate electrolyte that was used to render CFP hydrophilic. Additionally, we monitored the Fe 2p core level region for surface iron because iron is ubiquitous in glassware and many chemicals [85]; incidental iron contaminations would be detrimental for CO_2 reduction to useful carbon products because iron is an excellent hydrogen evolution electrocatalyst [86]. We highlighted the Fe 2p and K 2s core level binding energy regions in Fig. 5, according to values reported in the NIST XPS database [87]; these regions are 710–723 eV and 706–712 eV for Fe $2p_{1/2}$ and Fe $2p_{3/2}$, respectively, with a spin-orbit splitting

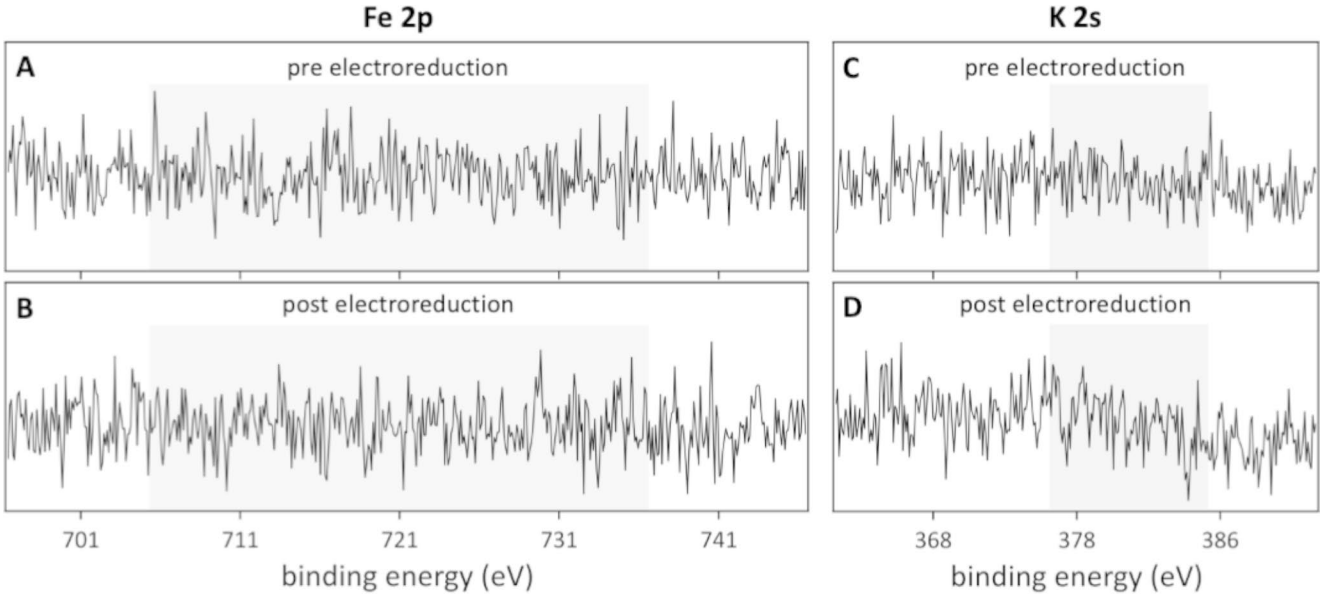

Fig. 5 High-resolution XPS data in the Fe 2p (A, B; highlighted in orange) and K 2s core level regions (C, D; highlighted in purple) of AuNP–CFP assemblies, collected before (A, C) and after citrate-removal electroreduction (B, D)

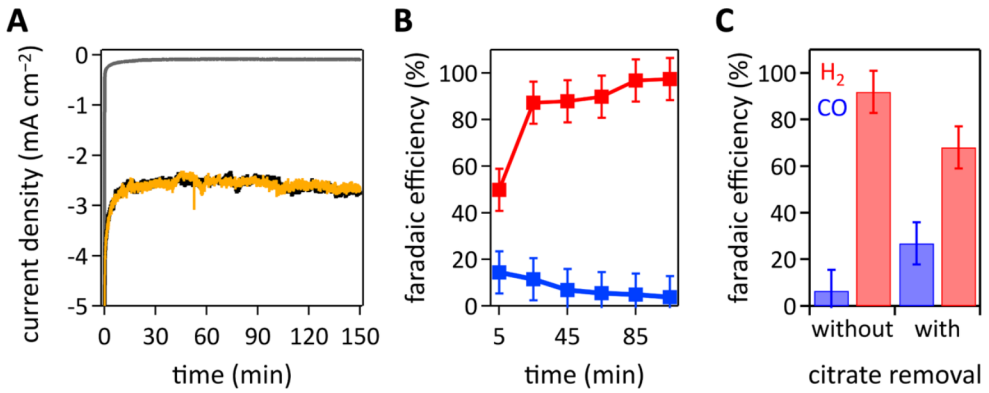

Fig. 6 Chronoamperometry data during CO_2 reduction electrocatalysis at an applied potential of −0.68 V vs. RHE in CO_2-saturated 0.1 M pH 6.8 $KHCO_3$ electrolyte (A); AuNP–CFP cathode without citrate removal, black, after a preceding citrate-removal electroreduction step, yellow, and neat hydrophilic CFP, gray. Time evolution of faradaic efficiencies of CO_2 reduction products H_2, red, and CO, blue, during electrocatalysis at a constant applied potential of −0.68 V vs. RHE using AuNP–CFP cathodes without citrate removal (B). Average faradaic efficiencies of CO and H_2 generated by CO_2 reduction at AuNP–CFP assemblies without or with citrate removal before CO_2 reduction electrocatalysis (C)

of 13.6 eV [88–91], and 376–385 eV for K 2s [92, 93]. Our XPS data show that neither iron nor potassium were present at AuNP–CFP assembly surfaces (Fig. 5).

Aqueous CO_2 reduction at AuNP–CFP cathodes. The AuNP–CFP assemblies served as working electrodes for CO_2 reduction electrocatalysis in CO_2-saturated aqueous 0.1 M pH 6.8 $KHCO_3$ electrolyte (Fig. 6). Carbon monoxide and hydrogen were the only detected products at an applied constant potential of −0.68 V vs. RHE. Neat hydrophilic CFP without gold nanoparticles generated negligible currents and no detectable products upon polarization at −0.68 V vs. RHE (Fig. 6A). Current generation during CO_2 reduction at AuNP–CFP assemblies remained virtually the same after a separate citrate-removal electroreduction step, compared to current generation at AuNP–CFP cathodes without electroreductive citrate removal (Fig. 6A), indicating that our electroreductive citrate removal indeed detached only citrate capping ligands from the gold nanoparticles and left the AuNP–CFP assemblies intact, as loss of gold active sites would have resulted in less current generation. Currents were stable for 2.5 h (Fig. 6A), indicating that AuNP–CFP assemblies were structurally stable after electroreductive removal of sodium citrate.

During chronoamperometry testing, currents first decayed steeply due to expected initial charging effects at the solid–liquid interface [94], followed by a brief shallower

decay, attributable to reductive citrate detachment, analog to the electroreductive citrate removal procedure. Assignment of this brief shallow decay to electroreductive citrate removal from gold surfaces is corroborated by the fact that the total faradaic efficiency at 5 min was less than 100% (Fig. 6B), as charge was lost in a material reduction process that did not contribute to CO_2 reduction product generation. Likewise, a similar brief shallow decay was observed with citrate-free AuNP–CFP cathodes, likely attributable to the reduction of Au_2O_3 that had formed in ambient air after the removal of citrate ligands, as detected by XPS (see above). After this induction period, currents were stable, indicating robust immobilization of gold nanoparticles on hydrophilic CFP.

We obtained a factor of 5.6 higher CO-to-H_2 ratio with AuNP–CFP assemblies, from which citrate was removed by a separate electroreduction step before CO_2 reduction electrocatalysis, than from analog AuNP–CFP cathodes without citrate removal (Fig. 6C). Citrate capping of gold nanoparticles has been reported to enhance hydrogen production [95], which explains the higher observed faradaic efficiency for hydrogen at citrate-capped AuNP–CFP electrodes. Taken together, our findings of virtually identical current generation at AuNP–CFP cathodes without and with a preceding citrate removal step (Fig. 6A), detection of adsorbed water at citrate-containing AuNP–CFP cathodes (Fig. 4A), and lower selectivity for CO at citrate-containing AuNP–CFP cathodes (Fig. 6C) suggest that the change in the microenvironment at the gold catalysts from citrate capped to bare gold by electroreductive citrate removal decreased the amount of surface water at the gold catalyst and concomitantly steered CO_2 reduction selectivity to higher faradaic efficiency for CO. Our observation of a significantly higher CO-to-H_2 ratio upon the removal of hydrophilic citrate corroborates the importance of water elimination at the catalyst surface for CO_2 reduction to useful carbon products. Therefore, in the following, all AuNP–CFP electrodes were first subjected to a separate electroreductive citrate removal step.

Higher current densities were obtained at AuNP–CFP cathodes at higher negative potentials, and CO-to-H_2 ratios first increased and then decreased as potentials became more negative (Fig. 7). Current densities were stable at all applied potentials, indicating robust immobilization of gold nanoparticles on hydrophilic CFP. The chronoamperometry data collected at applied potentials of − 1.1 and − 1.20 V vs. RHE exhibited features that we attribute to gas bubble formation at the working electrode (Fig. 7). In general, transport resistance increases while a gas bubble forms and grows at the electrode surface, resulting in decreased activity, ergo lower absolute measured current, until the bubble is released and the initial activity is restored, leading to characteristic oscillations in measured currents [96]. More bubble formation was observed at more negative applied potentials and concomitant more negative average currents (Fig. 7). Only hydrogen and carbon monoxide were detected as the products at applied constant potentials ranging from − 0.68 to − 1.20 V vs. RHE, and CO-to-H_2 ratios ranged from 1.89 to 0.16. Overall, our CO_2 reduction catalysis results demonstrate that hydrophilic CFP [22] is an excellent high surface area electrode substrate for assessing the performance of nanoparticulate electrocatalysts in aqueous electrolyte.

While CO_2 reduction electrocatalysis at nanostructured gold has been reported [7, 8, 42, 97–101], gold nanoparticles were in all these cases immobilized on gold surfaces because nanostructuring of gold is the easiest way to prepare macroscopic electrodes that contain gold nanoparticles. Gold nanoparticle CO_2 reduction catalysts have also been reported on metal oxide cathodes whose cost effectiveness

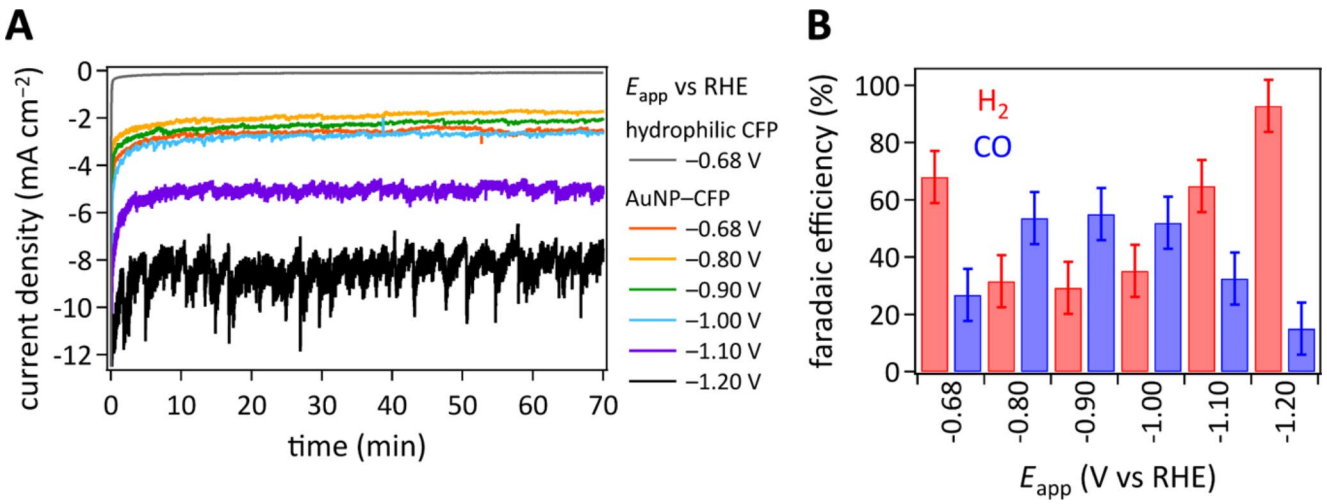

Fig. 7 Current densities at different controlled applied potentials E_{app} (A). Average faradaic efficiencies of CO and H_2 as a function of applied potential of aqueous CO_2 reduction catalyzed by AuNP–CFP cathodes (B)

and, more importantly, long-term stability under turnover are inherently challenging because metal oxides are redox active [102]. Our hydrophilic CFP [22] can serve a cost-effective electrode support for independently prepared gold nanoparticles. With an electrode size of 5.8 cm^2 and a gold loading of 10 µg cm^{-2}_{geo}, we used 58 µg Au in our AuNP–CFP assemblies. In contrast, a 0.025 mm thick Au foil of 5.8 cm^2 area weighs 280 mg; 0.025 mm is the minimum thickness required for mechanical stability in a liquid H-cell, as the one used here. As a result, our AuNP–CFP assemblies used > 4800× less gold by mass than would have been required with nanostructured gold foil. This material efficiency is particularly important because gold is a precious metal that is valued at >$63,000 per kg [103].

3.2 Preparation of Overlayers oAqueous CO_2 Reduction at AuNP–CFP Cathodes with Ionomer Overlayers

With the aim to control the CO-to-H_2 product ratio on gold nanoparticles independent of applied potential, we employed ion-conducting polymer overlayers consisting of Nafion or Sustainion. Commercial Nafion is superacidic (pK_a approximately − 6) [104], reducing the local pH environment at the catalyst. The sulfonic acid concentration of as-purchased Nafion 117 with respect to the polymer's density and equivalent weight is 1.13 M, and local acidities are even higher, because Nafion phase-separates into a hydrophobic phase that is concentrated on the −(CF_2)− backbone and hydrophilic SO_3^- clusters upon hydration; these sulfonate clusters are interconnected by channels that percolate through the polymer, which impart a percolation network for ionic conduction [47]. Highly acidic environments enhance hydrogen evolution in aqueous CO_2 reduction electrocatalysis [16]. Sustainion is moderately basic and designed for use with supporting electrolyte [105].

Surface basicity enhances CO_2 reduction via two processes, (i) promotion of the binding of CO_2 at the cathodic catalyst surface, for which the linear CO_2 molecule must bend to form the bond to the catalyst surface and accept the first electron in the reduction process [3, 16], and (ii) suppression of the competing proton reduction reaction to hydrogen. Additionally, local solution-phase basicity suppresses proton reduction. Engineering the catalyst microenvironment, for example by tailored overlayers, is preferable over use of alkaline electrolytes because (i) basicity is needed only in the close proximity of the catalyst surface, (ii) acidic aqueous electrolytes possess faster mass transport characteristics than alkaline water because protons are smaller than hydroxide ions [43], and (iii) CO_2 forms bicarbonate and carbonate in alkaline solutions, leading to inherent challenges with electrolyte neutralization [16]; catalyst fouling can also occur if the bicarbonates and carbonates are insoluble in the electrolyte.

Use of applied potential and concomitant current density to control the CO-to-H_2 product ratio has, in general, the disadvantage that at high negative bias H_2 production becomes dominant. At the same time, high negative bias is desirable because it produces higher current density. Therefore, we used a systematic series of ionomer overlayers to obtain desired CO-to-H_2 product ratios at the same applied current density.

We chose to assess the performance of AuNP–CFP assemblies with different ionomer overlayers at controlled current density because current generation is governed by the reaction kinetics and ergo a measure for faster turnover or, in other words, higher activity. Constant current experiments, also called chronopotentiometry or galvanostatic experiments, fix the current and concomitantly the kinetics, while the potentiostat varies the potential to maintain that current. Obtained potentials are, therefore, a measure of how much kinetic overpotential was needed to achieve a certain amount of kinetic turnover for CO_2 reduction at gold nanoparticles. If CO_2 reduction to CO occurs in the transport-limited regime, i.e. all CO_2 molecules that are present at the catalyst surface turn over to form CO, the control system of the potentiostat will make the potential increasingly negative to drive alternative reactions to meet the desired current; in the case of CO_2 reduction at gold surfaces the main competing reaction is hydrogen evolution, which is easily identifiable by product quantification by gas chromatography. In contrast, in a constant applied potential experiment, also called controlled potential, chronoamperometry, or potentiostatic experiment, the thermodynamic driving force is kept constant and the total electrocatalytic activity is measured through the current, which is comprised of convoluted contributions from CO and H_2 production. Ergo, galvanostatic data are more useful in the assessment of ionomer overlayers and concomitant microenvironment effects on gold catalysts in AuNP–CFP assemblies.

Gold cathodes produce only CO, H_2, and formate in aqueous CO_2 reduction [106], and thus simplify the systematic comparison of ionomer overlayers, compared to catalysts that generate a multitude of products [16, 86, 107]. Here, hydrogen and carbon monoxide comprised ≥ 99% of the products at an applied constant current of − 6 mA cm^{-2}, with the remainder of up to 1% formate, detected by NMR (Figure S4), in agreement with reported products [42, 108]. Recent work on layering proton and anion exchange ionomers on Cu and Ag cathodes showed increased CO_2 reduction selectivity towards desired products, while suppressing H_2 evolution [49]. Here, we used high surface area AuNP–CFP assemblies to enhance product generation, and we modified Nafion preparation procedures to steer product

selectivity to CO. We performed K^+-exchange of sulfonic acid protons in Nafion 117, using a modified reported procedure [61], to raise the local pH at gold surfaces and suppress hydrogen evolution. We employed two different concentrations of KOH (0.1 and 0.4 M) mixed in a 2/1 (v/v) ratio of Nafion/KOH; Nafion was at 5 wt% in solution. Ion exchange affects the ionomer structure and conductivity, and additionally has significant effects on charge distribution in the microenvironment of the catalyst surface, which affects binding energies and product selectivity [109]. We chose to increase the cation concentration compared to the work by Bell et al. [53] because it seemed unlikely that at 0.1 M alkali ion concentration, all protons in the ionomer were exchanged. Protons have a much higher free energy of hydration compared to K^+ because H^+ cations are smaller than K^+ cations, creating an entropic penalty for the protons to exchange with K^+ [110, 111]. Conversely, Nafion has a higher affinity for larger than for smaller alkali ions or for protons, due to the low charge density of sulfonate sites, along with the hydration energy of the counterion and the gains in entropic energy from released water upon alkali ion substitution in the ionomer [112]. We chose to increase the concentration of the alkali ion exchange solution, compared to reported work, because alkali ion uptake by Nafion is increased by use of a more concentrated alkali ion solution.

Our results suggest that use of the more concentrated KOH solution (0.4 M) led to K^+-exchanged Nafion with a higher local pH, as we obtained an increased CO_2 reduction selectivity toward CO, compared to AuNP–CFP assemblies with 0.1 M K^+-exchanged Nafion overlayers that were prepared by modifying a procedure reported in ref [61]. (Figures 8, 0.1 M vs. 0.4 M K^+-Nafion). We additionally used Sustainion for comparison, which is often used in CO_2 reduction electrocatalysis because it possesses a 20-fold increased solubility for CO_2 compared to water [49]. Further, we employed Cs^+-exchanged Nafion overlayers with four different Cs^+ concentrations on AuNP–CFP assemblies.

Since we used virtually identical AuNP–CFP assemblies and otherwise unchanged electrocatalysis conditions, we expected that CO_2 reduction catalysis occurred at gold nanoparticles, irrespective of the nature of the ionomer overlayer. Control experiments with ionomers on CFP without gold showed negligible CO_2 reduction products, and more negative potentials were needed to maintain a current of -6 mA cm^{-2} in galvanostatic experiments due to predominant hydrogen evolution (Figure S5). Additional potentiometric control experiments of CFP–AuNP assemblies with select ionomer overlayers at -0.68 V vs. RHE in N_2- instead of CO_2-saturated electrolyte showed no formate and negligible CO formation, low current generation, and low amounts of produced hydrogen that were close to the detection limit of the gas chromatograph of approximately 200 ppm for H_2 (Figure S6).

The chemical nature of ionomer overlayers affected the microenvironments at gold surfaces, especially with respect to local pH and CO_2 concentration. Comparison of AuNP–CFP assemblies with no, Nafion, K^+-exchanged Nafion, or Sustainion overlayers showed the following (Table 1): cathodes without any ionomer overlayer exhibited similarly high CO-to-H_2 ratios and similar measured potentials

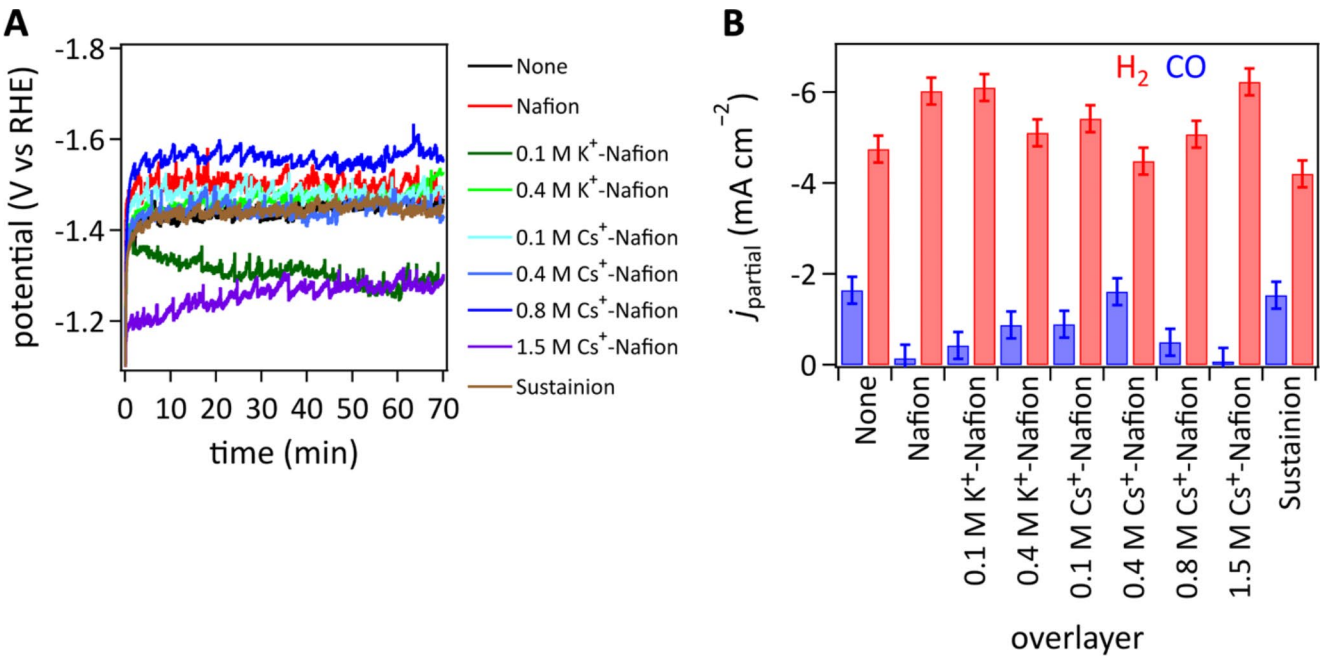

Fig. 8 Measured potentials in constant current experiments at -6 mA cm^{-2} as a function of overlayer materials (A). Partial current densities of CO and H_2 as a function of overlayer materials (B)

as AuNP–CFP assemblies with Sustainion overlayers; both suppressed hydrogen evolution to a greater extent than unexchanged Nafion or K^+-exchanged Nafion, even with use of the 0.4 M K^+ cation solution. In comparisons of measured potentials, lower absolute value of potential is better because less negative potential translates into less energy consumption to reach the preset current density. Assemblies of AuNP–CFP with unexchanged Nafion overlayers produced mostly hydrogen, as expected for a highly acidic microenvironment of gold nanoparticles.

In addition to using K^+-exchanged Nafion overlayers, we employed Cs^+-exchanged Nafion overlayers on AuNP–CFP assemblies because Cs^+ cations are expected to enhance local concentrations of CO_2 at the catalyst surface more than K^+ cations. Since Cs^+ cations have a larger ionic radius than K^+ cations, the radius of hydration of Cs^+ is smaller than that of K^+. Hence, Cs^+ cations induce a higher surface-charge density that creates a stronger electrostatic field in the double layer, which stabilizes the adsorbed CO_2 [113, 114]. Analog to our experiments with K^+-exchanged Nafion, we increased the Cs^+ cation concentration in the exchange solution, compared to the work by Bell et al. [53], because at low Cs^+ concentration in the exchange solution, the amount of cation exchange may not be sufficient [110, 111]. We chose Cs^+ cation concentrations in the exchange solution of 0.1 M (as Bell et al. [53]), 0.4, 0.8, and 1.5 M.

Assemblies of AuNP–CFP with 0.4 M Cs^+-exchanged Nafion overlayers performed best amongst all cathodes, exhibiting the highest CO-to-H_2 ratio of 0.36:1 and a measured potential of − 1.43 V vs. RHE at a constant applied current density of − 6 mA cm^{-2}. Use of 0.1 M Cs^+-exchanged Nafion overlayers has been reported [53]; we found that 0.4 M Cs^+-exchanged Nafion overlayers increased CO selectivity by more than a factor of 2, compared to 0.1 M Cs^+-exchanged Nafion overlayers. Concentrations of Cs^+ cations of greater than 0.4 M in the exchange solution significantly decreased CO production to below 10% with respect to generated hydrogen.

Table 1 Carbon dioxide reduction performance of AuNP–CFP assemblies as a function of the nature of ionomer overlayers

Overlayer	CO-to-H_2 ratio	Potential at − 6 mA cm^{-2} (V vs. RHE)
None	0.35:1	–1.42
Sustainion	0.36:1	–1.44
Unexchanged Nafion	0.03:1	–1.50
0.1 M K^+-exchanged Nafion	0.07:1	–1.33
0.4 M K^+-exchanged Nafion	0.17:1	–1.45
0.1 M Cs^+-exchanged Nafion	0.17:1	–1.49
0.4 M Cs^+-exchanged Nafion	0.36:1	–1.43
0.8 M Cs^+-exchanged Nafion	0.09:1	–1.55
1.5 M Cs^+-exchanged Nafion	0.01:1	–1.25

Strikingly, the best-performing cathodes, i.e. AuNP–CFP assemblies with no, Sustainion, or 0.4 M Cs^+-exchanged Nafion overlayers (Table 1), exhibited virtually the same performance for CO_2 reduction in 0.1 M aqueous $KHCO_3$ buffer. Sustainion has a 20-fold higher solubility for CO_2 than water [49], which comprised the microenvironment of the AuNP–CFP assemblies with no overlayer, suggesting that at all of these three cathodes, CO_2 mass transport did not limit the CO_2 reduction reaction. We surmise that the ratio of ca. 0.36:1 is indicative of the intrinsic rate constants of CO vs. H_2 production at gold nanoparticle surfaces.

While CO production was half of that of AuNP-CFP assemblies with 0.4 M Cs^+-exchanged Nafion, cathodes with 0.4 M K^+-exchanged or 0.1 M Cs^+-exchanged Nafion showed remarkably similar performance (Table 1), presumably because the smaller hydrated Cs^+ cations outperformed the larger hydrated K^+ cations, while the exchange solution with lower alkali ion concentration led to less ion exchange, balancing the overall performance. Based on our results of best performance with 0.4 M Cs^+-exchanged Nafion, we conclude that CO_2 mass transport into the double layer likely limited the CO_2 reduction reaction at AuNP–CFP assemblies with 0.4 M K^+-exchanged or 0.1 M Cs^+-exchanged Nafion overlayers.

Cathodes with unexchanged or 0.1 M K^+-exchanged Nafion overlayers predominantly produced hydrogen in 0.1 M CO_2-saturated aqueous $KHCO_3$ buffer. High hydrogen generation from AuNP–CFP assemblies with unexchanged Nafion overlayers is unsurprising because of the high acidity of Nafion [104] that reduces the local pH environment at the catalyst, presumably preventing CO_2 adsorption at the catalyst surface, as surface basicity is needed for CO_2 to bind at catalyst surface sites [3, 16]. Surface starvation of CO_2 leaves only H_2 production by proton or bicarbonate reduction to maintain the set current in galvanostatic experiments, leading to an observed potential of − 1.50 V vs. RHE to maintain a current density of − 6 mA cm^{-2}, the second most negative observed potential at AuNP–CFP assemblies, which we rationally designed to have high overpotentials for hydrogen evolution. Cathodes with 0.1 M K^+-exchanged Nafion also produced predominantly H_2, but product generation had twice the selectivity for CO and occurred at an observed potential that was 0.17 V less negative, compared to unexchanged Nafion (Table 1). Adsorption of CO_2 strongly depends on the electric field in the double layer [115]. The presence of alkaline cations in the double layer increase the interfacial electric field and decrease the energy barrier for CO_2 adsorption on gold [115], increasing selectivity for CO. The dominant dipole field contribution of cations on gold surfaces has recently been ascribed to the Onsager reaction field, which is generally produced by a solute dipole polarizing the surrounding solvent and ions; in the case of CO_2, the

dipole induced by CO_2 bending produces a larger electric field than the Stern layer electric field in the electrochemical double layer [116, 117]. Irrespective of the physical origin of the electric field enhancement, alkali cations at the gold catalyst–electrolyte interface increase CO selectivity. In addition, alkali cations promote bicarbonate reduction to H_2 at gold surfaces with lower overpotential than proton reduction to H_2 [118], explaining why we observed a potential difference of 0.17 V for AuNP–CFP assemblies with unexchanged vs. 0.1 M K^+-exchanged Nafion overlayers. Only the K^+-exchanged Nafion enabled bicarbonate reduction, thus lowering the overpotential for H_2 generation, whereas the absence of alkali cations in unexchanged Nafion disfavored bicarbonate reduction, so that current was generated by proton reduction to H_2, which necessitated a high potential to overcome the rationally designed high overpotential for proton reduction at AuNP–CFP cathodes.

Predominant hydrogen evolution at AuNP–CFP assemblies with 0.8 or 1.5 M Cs^+-exchanged Nafion overlayers was likely due to disrupted transport of ions, water, and CO_2 in Nafion that was exposed to solutions with high alkali cation concentrations [119]. Transport of CO_2 occurs mainly through the hydrophilic domains in Nafion [120]. In Nafion, water affinity and ionomer hydration drive the phase segregation and percolation network morphology, which facilitates the excellent transport properties of Nafion ionomers [47]. High alkali content in the ionomer decreases water affinity. The percolation threshold is not met with low ionomer hydration, and mass transport decreases because of a lack of interconnected hydrophilic domains [119]. High alkali concentrations in an exchange solution significantly lower the water content within the Nafion ionomer during drying, which is needed to create an overlayer, and concomitantly decrease the extent and number of hydrophilic domains [121]. Additionally, high Cs^+ concentrations in Nafion enable detrimental CO_2 capture by forming $CsHCO_3$, which limits the availability of CO_2 for reduction to useful carbon products [120]. While it is possible to reduce bicarbonate instead of CO_2, bicarbonate reduction to carbon products is generally energetically less favorable than CO_2 reduction [122]. However, alkali cations, such as Cs^+, promote bicarbonate reduction to H_2 at gold surfaces with lower overpotential than proton reduction to H_2 [118], explaining why we observed the lowest selectivity for CO together with the least negative potential of − 1.25 V vs. RHE at AuNP–CFP assemblies with 1.5 M Cs^+-exchanged Nafion overlayers; in contrast, AuNP–CFP assemblies with 0.8 M Cs^+-exchanged Nafion overlayers exhibited the most negative observed potential. All phenomena together rationalize why AuNP–CFP assemblies with 0.8 or 1.5 M Cs^+-exchanged Nafion overlayers produced CO-to-H_2 ratios that were decreased by a factor of 4 or 36, respectively, compared to our best-performing cathodes that consisted of AuNP–CFP assemblies with 0.4 M Cs^+-exchanged Nafion overlayers.

Overall, we observed almost identical performance by 0.4 M Cs^+-exchanged Nafion and Sustainion ionomer overlayers on AuNP–CFP cathodes. We note that 0.4 M Cs^+-exchanged Nafion is a cation exchange ionomer, whereas the popular Sustainion is an anion exchange ionomer. If an anionic intermediate, such as formate, is required to reside near the cathode surface for downstream reductive C–C-coupling, as has been suggested for Ni_2P catalysts [123], a cation exchange ionomer overlayer, such as our 0.4 M Cs^+-exchanged Nafion, is advantageous because an anion exchange ionomer will readily shuttle anions away from the catalyst surface, thus preventing subsequent C–C-coupling. Hence, our work provides a beneficial alternative to existing ionomers toward CO_2 reduction to upgraded chemicals and fuels.

4 Conclusions

Our universal approach solved the long-standing challenge of providing inexpensive, hydrophilic, high surface area carbon substrates for nanoparticulate payloads for use in aqueous media. We immobilized gold nanoparticles from aqueous colloid on hydrophilic CFP and applied these high surface area assemblies as cathodes in aqueous carbon dioxide reduction electrocatalysis. Uniform gold nanoparticle distributions on carbon fibers, stable electrocatalytic current generation, and reduction of CO_2 to CO and H_2 indicated that immobilization of gold nanoparticles was successful; a factor of > 4800 less gold was used than would have been needed with traditionally used gold nanoparticles on gold foil.

We engineered gold catalyst microenvironments, predicated on the key design criteria for CO_2 reduction to useful carbon products, namely (i) elimination of water at the catalyst surface to suppress H_2 evolution, (ii) enhancement of mass transport of CO_2 molecules to the catalyst surface, and (iii) facilitating CO_2 binding and bending at the cathodic catalyst surface upon the first electron transfer, to form the surface-bound C–O intermediate. XPS data of AuNP–CFP cathodes that were subjected before CO_2 reduction to a separate citrate-removal electroreduction step provided evidence for enhanced amounts of bare surface gold and beneficial loss of adsorbed water upon detachment of citrate capping ligands; CO-to-H_2 ratios at citrate-free AuNP–CFP cathodes were a factor of 5.6 higher than at citrate-capped AuNP–CFP electrodes, corroborating the importance of water elimination at the catalyst surface.

We succeeded in controlling CO-to-H_2 ratios by applied potentials and ionomer overlayers, to produce clean syngas with tailored relative proportions of CO and H_2. AuNP–CFP assemblies with Sustainion or 0.4 M Cs^+-exchanged Nafion overlayers exhibited virtually the same performance for CO_2 reduction in 0.1 M aqueous $KHCO_3$ buffer. We observed a CO:H_2 ratio of 0.36:1 at these best-performing cathodes, indicative of the intrinsic rate constants of CO vs. H_2 production at gold nanoparticle surfaces. Our finding that AuNP–CFP cathodes with the *cation* exchange ionomer 0.4 M Cs^+-exchanged Nafion performed as well as AuNP–CFP assemblies with the *anion* exchange ionomer Sustainion paves the way for downstream reductive C–C-coupling at CO_2 reduction catalysts whose mechanisms proceed through anionic intermediates, such as formate, because only the cation exchange ionomer enables long residence times of anionic intermediates in the catalyst microenvironment, whereas the anion exchange ionomer Sustainion would readily shuttle anions away from the catalyst surface, thus preventing subsequent C–C-coupling transformations.

Our systematic series of K^+- and Cs^+-exchanged Nafion overlayers revealed the mechanistic underpinnings of CO selectivity as a function of microenvironments at AuNP–CFP catalyst surfaces. Overall, our results highlight the exceptional utility of hydrophilic CFP–nanocatalyst assemblies for sustainable processes.

Abbreviations

AuNP	Gold nanoparticle
CFP	Carbon fiber paper
EDX	Energy-dispersive X-ray
FE	Faradaic efficiency
Geo	Geometric
Prod.	Product
RHE	Reversible hydrogen electrode
SDS	Sodium dodecyl sulfate
SEM	Scanning electron microscopy
XPS	X-ray photoelectron spectroscopy

Supplementary Information The online version contains supplementary material available at https://doi.org/10.1007/s11244-023-01850-3.

Acknowledgements Acknowledgment is made to the Donors of the American Chemical Society Petroleum Research Fund for support of this research (grant number 62578-DNI5). We are grateful for start-up funds from the University of Rochester. We acknowledge Prof. T. F. Jaramillo (Stanford University) for providing a CO_2 reduction electrochemical cell.

References

1. Forsythe RC, Cox CP, Wilsey MK, Müller AM (2021) Pulsed laser in Liquids made nanomaterials for Catalysis. Chem Rev 121(13):7568–7637. https://doi.org/10.1021/acs.chemrev.0c01069
2. Taseska T, Yu W, Wilsey MK, Meng Z, Cox CP, Ngarnim SS, Müller AM (2023) Analysis of the scale of Global Human needs and Opportunities for sustainable Catalytic Technologies. Top Catal 66(5–8):338–374. https://doi.org/10.1007/s11244-023-01799-3
3. Wilsey MK, Cox CP, Forsythe RC, McCarney LR, Müller AM (2021) Selective CO2 reduction towards a single upgraded product: a minireview on multi-elemental copper-free electrocatalysts. Catal Sci Technol 11(2):416–424. https://doi.org/10.1039/d0cy02010a
4. Siahrostami S, Jiang K, Karamad M, Chan K, Wang H, Nørskov J (2017) Theoretical investigations into defected graphene for Electrochemical reduction of CO2. ACS Sustain Chem Eng 5(11):11080–11085. https://doi.org/10.1021/acssuschemeng.7b03031
5. Higgins D, Hahn C, Xiang C, Jaramillo TF, Weber AZ (2018) Gas-diffusion electrodes for carbon dioxide reduction: a new paradigm. ACS Energy Lett 4(1):317–324
6. Cave ER, Montoya JH, Kuhl KP, Abram DN, Hatsukade T, Shi C, Hahn C, Nørskov JK, Jaramillo TF (2017) Electrochemical CO 2 reduction on au surfaces: mechanistic aspects regarding the formation of major and minor products. Phys Chem Chem Phys 19(24):15856–15863
7. Zhao S, Jin R, Jin R (2018) Opportunities and Challenges in CO2 reduction by gold- and silver-based Electrocatalysts: from Bulk Metals to Nanoparticles and Atomically Precise Nanoclusters. ACS Energy Lett 3(2):452–462. https://doi.org/10.1021/acsenergylett.7b01104
8. Goyal A, Marcandalli G, Mints VA, Koper MTM (2020) Competition between CO2 reduction and hydrogen evolution on a gold electrode under Well-Defined Mass Transport Conditions. J Am Chem Soc 142(9):4154–4161. https://doi.org/10.1021/jacs.9b10061
9. Fischer F, Tropsch H (1923) The preparation of synthetic oil mixtures (synthol) from carbon monoxide and hydrogen. Brennstoff-Chem 4:276–285
10. Pan X, Jiao F, Miao D, Bao X (2021) Oxide–zeolite-based Composite Catalyst Concept that enables Syngas Chemistry beyond Fischer–Tropsch Synthesis. Chem Rev 121(11):6588–6609. https://doi.org/10.1021/acs.chemrev.0c01012
11. Schlögl R (2022) Chemical Energy Storage, 2nd edn. De Gruyter, Berlin, Germany. https://doi.org/10.1515/9783110608458
12. Syngas Composition (2023) National Energy Technology Laboratory. http://www.netl.doe.gov/research/coal/energy-systems/gasification/gasifipedia/syngas-composition. Accessed April 3,
13. Yang N, Waldvogel SR, Jiang X (2016) Electrochemistry of Carbon Dioxide on Carbon Electrodes. ACS Appl Mater Interfaces 8(42):28357–28371. https://doi.org/10.1021/acsami.5b09825

14. Yang N, Swain GM, Jiang X (2016) Nanocarbon electrochemistry and electroanalysis: current status and future perspectives. Electroanalysis 28(1):27–34
15. Kakhki RM (2019) A review to recent developments in modification of carbon fiber electrodes. Arab J Chem 12(7):1783–1794
16. Nitopi S, Bertheussen E, Scott SB, Liu X, Engstfeld AK, Horch S, Seger B, Stephens IEL, Chan K, Hahn C, Nørskov JK, Jaramillo TF, Chorkendorff I (2019) Progress and Perspectives of Electrochemical CO2 reduction on copper in Aqueous Electrolyte. Chem Rev 119(12):7610–7672. https://doi.org/10.1021/acs.chemrev.8b00705
17. Sun Z, Hu Y, Zhou D, Sun M, Wang S, Chen W (2021) Factors influencing the performance of copper-bearing catalysts in the CO2 reduction system. ACS Energy Lett 6(11):3992–4022
18. Wang L, Chen W, Zhang D, Du Y, Amal R, Qiao S, Wu J, Yin Z (2019) Surface strategies for catalytic CO2 reduction: from two-dimensional materials to nanoclusters to single atoms. Chem Soc Rev 48(21):5310–5349
19. Wang X, Zhao Q, Yang B, Li Z, Bo Z, Lam KH, Adli NM, Lei L, Wen Z, Wu G (2019) Emerging nanostructured carbon-based non-precious metal electrocatalysts for selective electrochemical CO2 reduction to CO. J Mater Chem A 7(44):25191–25202
20. Hui SR, Shaigan N, Neburchilov V, Zhang L, Malek K, Eikerling M, Luna PD (2020) Three-dimensional cathodes for electrochemical reduction of CO2: from macro-to nano-engineering. Nanomaterials 10(9):1884
21. Mustafa A, Lougou BG, Shuai Y, Wang Z, Razzaq S, Shagdar E, Zhao J, Shan J (2021) Recent progresses in the mechanism, performance, and fabrication methods of metal-derived nanomaterials for efficient electrochemical CO2 reduction. J Mater Chem A 9(8):4558–4588
22. Wilsey MK, Watson KR, Fasusi OC, Yegela BP, Cox CP, Raffaelle PR, Cai L, Müller AM (2023) Selective hydroxylation of Carbon Fiber Paper for Long-Lasting hydrophilicity by a Green Chemistry process. Adv Mater Interfaces 10(2):2201684. https://doi.org/10.1002/admi.202201684
23. Wang X, Li W, Xiong D, Petrovykh DY, Liu L (2016) Bifunctional Nickel Phosphide Nanocatalysts supported on Carbon Fiber Paper for highly efficient and stable overall water splitting. Adv Funct Mater 26(23):4067–4077. https://doi.org/10.1002/adfm.201505509
24. Thangavel P, Kim G, Kim KS (2021) Electrochemical integration of amorphous NiFe (oxy)hydroxides on surface-activated carbon fibers for high-efficiency oxygen evolution in alkaline anion exchange membrane water electrolysis. J Mater Chem A 9(24):14043–14051. https://doi.org/10.1039/d1ta02883a
25. Huang Z, Ji Z, Yin P, Shu Y, Xu Q, Hu X-Y (2019) Salicylic acid impregnated activated carbon fiber paper: an effective platform for the simple and sensitive detection of hydroxyl radicals in the atmosphere. Electrochem Commun 100:113–116. https://doi.org/10.1016/j.elecom.2019.02.008
26. Yang H, Zhao J, Qiu M, Sun P, Han D, Niu L, Cui G (2019) Hierarchical bi-continuous pt decorated nanoporous Au-Sn alloy on carbon fiber paper for ascorbic acid, dopamine and uric acid simultaneous sensing. Biosens Bioelectron 124–125:191–198. https://doi.org/10.1016/j.bios.2018.10.012
27. Kong W, Wang G, Zhang M, Duan X, Hu J, Duan X (2019) Villiform carbon fiber paper as current collector for capacitive deionization devices with high areal electrosorption capacity. Desalination 459:1–9. https://doi.org/10.1016/j.desal.2019.02.016
28. Coelho IF, Barbosa JR, Liu L, de Nogueira SC, Franceschini C, Ponzio DF, Silva EA, Xing JCM Y (2020) Nickel nanoparticles supported by commercial carbon paper as a catalyst for urea electro-oxidation. Mater Renew Sustain Energy 9(3):1–11
29. Xu S, Jiang Q (2018) Surface modification of carbon fiber support by ferrous oxalate for biofilm wastewater treatment system. J Clean Prod 194:416–424. https://doi.org/10.1016/j.jclepro.2018.05.159
30. Ponchon JL, Cespuglio R, Gonon F, Jouvet M, Pujol JF (1979) Normal pulse polarography with carbon fiber electrodes for in vitro and in vivo determination of catecholamines. Anal Chem 51(9):1483–1486. https://doi.org/10.1021/ac50045a030
31. Torrinha Á, Morais S (2021) Electrochemical (bio)sensors based on carbon cloth and carbon paper: an overview. Trends Anal Chem 142:1–12. https://doi.org/10.1016/j.trac.2021.116324
32. Khanna R, Cayumil R (2018) Recent developments in the field of Carbon fibers. BoD–Books on Demand, Online
33. Saito N, Aoki K, Usui Y, Shimizu M, Hara K, Narita N, Ogihara N, Nakamura K, Ishigaki N, Kato H (2011) Application of carbon fibers to biomaterials: a new era of nano-level control of carbon fibers after 30-years of development. Chem Soc Rev 40(7):3824–3834
34. Mueller AM, Wilsey MK, Watson KR, Fasusi OC, Yegela BP, Cox CP (2022) Acid-free solution process for structurally intact carbon fiber paper with long-lasting hydrophilicity. Patent Pending.
35. Benson EE, Kubiak CP, Sathrum AJ, Smieja JM (2009) Electrocatalytic and homogeneous approaches to conversion of CO2 to liquid fuels. Chem Soc Rev 38(1):89–99
36. Morris AJ, Meyer GJ, Fujita E (2009) Molecular approaches to the photocatalytic reduction of carbon dioxide for solar fuels. Acc Chem Res 42(12):1983–1994
37. Liu C, Colón BC, Ziesack M, Silver PA, Nocera DG (2016) Water splitting–biosynthetic system with CO2 reduction efficiencies exceeding photosynthesis. Science 352(6290):1210–1213
38. Dogutan DK, Nocera DG (2019) Artificial photosynthesis at efficiencies greatly exceeding that of natural photosynthesis. Acc Chem Res 52(11):3143–3148
39. Leung KY, McCrory CC (2019) Effect and prevention of trace ag + contamination from Ag/AgCl reference electrodes on CO2 reduction product distributions at polycrystalline copper electrodes. ACS Appl Energy Mater 2(11):8283–8293
40. Liu Y, McCrory CC (2019) Modulating the mechanism of electrocatalytic CO2 reduction by cobalt phthalocyanine through polymer coordination and encapsulation. Nat Commun 10(1):1–10
41. Ostericher AL, Porter TM, Reineke MH, Kubiak CP (2019) Thermodynamic targeting of electrocatalytic CO 2 reduction: advantages, limitations, and insights for catalyst design. Dalton Trans 48(42):15841–15848
42. Zhang BA, Costentin C, Nocera DG (2019) On the conversion efficiency of CO2 electroreduction on gold. Joule 3(7):1565–1568
43. Forsythe RC, Müller AM (2022) Quo vadis water oxidation? Catal Today 388–389:329–332. https://doi.org/10.1016/j.cattod.2020.06.011
44. Robert M, Daasbjerg K, Constentin C (2020) Carbon Dioxide Electrochemistry. Royal Society of Chemistry, London, U.K
45. Barrett JA, Miller CJ, Kubiak CP (2021) Electrochemical reduction of CO2 using Group VII Metal catalysts. Trends Chem 3(3):176–187
46. Wang L, Liu H, Konik RM, Misewich JA, Wong SS (2013) Carbon nanotube-based heterostructures for solar energy applications. Chem Soc Rev 42(20):8134–8156
47. Mauritz KA, Moore RB (2004) State of understanding of Nafion. Chem Rev 104(10):4535–4586
48. García de Arquer FP, Dinh C-T, Ozden A, Wicks J, McCallum C, Kirmani AR, Nam D-H, Gabardo C, Seifitokaldani A, Wang X (2020) CO2 electrolysis to multicarbon products at activities greater than 1 a cm – 2. Science 367(6478):661–666
49. Bui JC, Kim C, King AJ, Romiluyi O, Kusoglu A, Weber AZ, Bell AT (2022) Engineering Catalyst–Electrolyte Microenvironments to optimize the activity and selectivity for the Electrochemical reduction of CO2 on Cu and Ag. Acc Chem Res 55(4):484–494. https://doi.org/10.1021/acs.accounts.1c00650

50. Salvatore DA, Gabardo CM, Reyes A, O'Brien CP, Holdcroft S, Pintauro P, Bahar B, Hickner M, Bae C, Sinton D (2021) Designing anion exchange membranes for CO2 electrolysers. Nat Energy 6(4):339–348
51. Yang H, Kaczur JJ, Sajjad SD, Masel RI (2017) Electrochemical conversion of CO2 to formic acid utilizing Sustainion™ membranes. J CO2 Utilization 20:208–217
52. Kaczur JJ, Yang H, Liu Z, Sajjad SD, Masel RI (2020) A review of the use of immobilized ionic liquids in the electrochemical conversion of CO2. C 6(2):33
53. Kim C, Bui JC, Luo X, Cooper JK, Kusoglu A, Weber AZ, Bell AT (2021) Tailored catalyst microenvironments for CO2 electroreduction to multicarbon products on copper using bilayer ionomer coatings. Nat Energy 6(11):1026–1034
54. Delacourt C, Ridgway PL, Kerr JB, Newman J (2007) Design of an electrochemical cell making syngas (CO + H2) from CO2 and H2O reduction at room temperature. J Electrochem Soc 155(1):B42. https://doi.org/10.1149/1.2801871
55. Andrews E, Katla S, Kumar C, Patterson M, Sprunger P, Flake J (2015) Electrocatalytic reduction of CO2 at au nanoparticle electrodes: Effects of Interfacial Chemistry on Reduction Behavior. J Electrochem Soc 162(12):F1373. https://doi.org/10.1149/2.0541512jes
56. Gupta K, Bersani M, Darr JA (2016) Highly efficient electroreduction of CO2 to formic acid by nano-copper. J Mater Chem A 4(36):13786–13794. https://doi.org/10.1039/c6ta04874a
57. Pan H, Barile CJ (2020) Electrochemical CO2 reduction to methane with remarkably high faradaic efficiency in the presence of a proton permeable membrane. Energy Environ Sci 13(10):3567–3578. https://doi.org/10.1039/d0ee02189j
58. Wang M, Wan L, Luo J (2021) Promoting CO2 electroreduction on CuO nanowires with a hydrophobic nafion overlayer. Nanoscale 13(6):3588–3593. https://doi.org/10.1039/d0nr08369k
59. Kim YE, Lee W, Ko YN, Park JE, Tan D, Hong J, Jeon YE, Oh J, Park KT (2022) Role of Binder in Cu2O Gas Diffusion Electrodes for CO2 reduction to C2 + products. ACS Sustainable Chem Eng 10(36):11710–11718. https://doi.org/10.1021/acssuschemeng.2c03915
60. Chang M, Ren W, Ni W, Lee S, Hu X (2023) Ionomers modify the selectivity of Cu-Catalyzed Electrochemical CO2 reduction. Chemsuschem 16(5):e202201687. https://doi.org/10.1002/cssc.202201687
61. Suntivich J, Gasteiger HA, Yabuuchi N, Shao-Horn Y (2010) Electrocatalytic measurement methodology of oxide catalysts using a thin-film rotating disk electrode. J Electrochem Soc 157(8):B1263–B1268. https://doi.org/10.1149/1.3456630
62. Barr TL, Seal S (1995) Nature of the use of adventitious carbon as a binding energy standard. J Vac Sci Technol A 13(3):1239–1246. https://doi.org/10.1116/1.579868
63. Shirley DA (1972) High-resolution X-Ray Photoemission Spectrum of the Valence bands of gold. Phys Rev B 5(12):4709–4714
64. Kuhl KP, Cave ER, Abram DN, Jaramillo TF (2012) New insights into the electrochemical reduction of carbon dioxide on metallic copper surfaces. Energy Environ Sci 5(5):7050–7059. https://doi.org/10.1039/C2EE21234J
65. Sinclair TS, Gray HB, Müller AM (2018) Photoelectrochemical performance of BiVO4 Photoanodes Integrated with [NiFe]-Layered double hydroxide nanocatalysts. Eur J Inorg Chem 2018:1060–1067. https://doi.org/10.1002/ejic.201701231
66. Yi Y, Weinberg G, Prenzel M, Greiner M, Heumann S, Becker S, Schlögl R (2017) Electrochemical corrosion of a glassy carbon electrode. Catal Today 295:32–40. https://doi.org/10.1016/j.cattod.2017.07.013
67. Nigrovski B, Scholz P, Krech T, Qui NV, Pollok K, Keller T, Ondruschka B (2009) The influence of microwave heating on the texture and catalytic properties of oxidized multi-walled carbon nanotubes. Catal Commun 10(11):1473–1477. https://doi.org/10.1016/j.catcom.2009.03.023
68. Datsyuk V, Kalyva M, Papagelis K, Parthenios J, Tasis D, Siokou A, Kallitsis I, Galiotis C (2008) Chemical oxidation of multiwalled carbon nanotubes. Carbon 46(6):833–840. https://doi.org/10.1016/j.carbon.2008.02.012
69. Utsumi S, Honda H, Hattori Y, Kanoh H, Takahashi K, Sakai H, Abe M, Yudasaka M, Iijima S, Kaneko K (2007) Direct evidence on C – C single bonding in single-wall carbon nanohorn aggregates. J Phys Chem C 111(15):5572–5575
70. Desimoni E, Casella G, Morone A, Salvi A (1990) XPS determination of oxygen-containing functional groups on carbon-fibre surfaces and the cleaning of these surfaces. Surf Interface Anal 15(10):627–634
71. Desimoni E, Casella GI, Salvi AM, Cataldi TRI, Morone A (1992) XPS investigation of ultra-high-vacuum storage effects on carbon fibre surfaces. Carbon 30(4):527–531. https://doi.org/10.1016/0008-6223(92)90171-R
72. Tsai H, Hu E, Perng K, Chen M, Wu J-C, Chang Y-S (2003) Instability of gold oxide Au2O3. Surf Sci 537(1):L447–L450. https://doi.org/10.1016/S0039-6028(03)00640-X
73. Stadnichenko A, Koshcheev S, Boronin A (2015) An XPS and TPD study of gold oxide films obtained by exposure to RF-activated oxygen. J Struct Chem 56(3):557–565
74. Higo M, Matsubara Y, Kobayashi Y, Mitsushio M, Yoshidome T, Nakatake S (2020) Formation and decomposition of gold oxides prepared by an oxygen-dc glow discharge from gold films and studied by X-ray photoelectron spectroscopy. Thin Solid Films 699:137870
75. Chenakin SP, Kruse N (2016) Au 4f spin–orbit coupling effects in supported gold nanoparticles. Phys Chem Chem Phys 18(33):22778–22782
76. Sahoo SR, Ke S-C (2021) Spin-Orbit Coupling Effects in au 4f core-level electronic structures in supported low-dimensional gold nanoparticles. Nanomaterials 11(2):554
77. Patanen M, Aksela S, Urpelainen S, Kantia T, Heinäsmäki S, Aksela H (2011) Free atom 4f photoelectron spectra of au, pb, and Bi. J Electron Spectrosc Relat Phenom 183(1–3):59–63
78. Anderson DP, Alvino JF, Gentleman A, Al Qahtani H, Thomsen L, Polson MI, Metha GF, Golovko VB, Andersson GG (2013) Chemically-synthesised, atomically-precise gold clusters deposited and activated on titania. Phys Chem Chem Phys 15(11):3917–3929
79. Caprile L, Cossaro A, Falletta E, Della Pina C, Cavalleri O, Rolandi R, Terreni S, Ferrando R, Rossi M, Floreano L (2012) Interaction of L-cysteine with naked gold nanoparticles supported on HOPG: a high resolution XPS investigation. Nanoscale 4(24):7727–7734
80. Ono LK, Roldan Cuenya B (2008) Formation and thermal stability of Au2O3 on gold nanoparticles: size and support effects. J Phys Chem C 112(12):4676–4686
81. Vitale F, Fratoddi I, Battocchio C, Piscopiello E, Tapfer L, Russo MV, Polzonetti G, Giannini C (2011) Mono-and bi-functional arenethiols as surfactants for gold nanoparticles: synthesis and characterization. Nanoscale Res Lett 6:1–9
82. Asami K (1976) A precisely consistent energy calibration method for X-ray photoelectron spectroscopy. J Electron Spectrosc Relat Phenom 9(5):469–478
83. Thomas TD, Weightman P (1986) Valence electronic structure of AuZn and AuMg alloys derived from a new way of analyzing auger-parameter shifts. Phys Rev B 33(8):5406
84. Juodkazis K, Juodkazyt J, Jasulaitien V, Lukinskas A, Šebeka B (2000) XPS studies on the gold oxide surface layer formation. Electrochem Commun 2(7):503–507
85. Trotochaud L, Young SL, Ranney JK, Boettcher SW (2014) Nickel-Iron Oxyhydroxide Oxygen-Evolution Electrocatalysts:

the role of intentional and Incidental Iron Incorporation. J Am Chem Soc 136(18):6744–6753. https://doi.org/10.1021/ja502379c
86. Hori Y, Wakebe H, Tsukamoto T, Koga O (1994) Electrocatalytic process of CO Selectivity in Electrochemical reduction of CO2 at Metal Electrodes in Aqueous Media. Electrochim Acta 39(11–12):1833–1839. https://doi.org/10.1016/0013-4686(94)85172-7
87. National Institute of Standards and Technology (2012) NIST X-ray Photoelectron Spectroscopy Database 20, Version 4.1. Gaithersburg, U.S.A. http://srdata.nist.gov/xps/ Accessed April, 2022
88. Hawn DD, DeKoven BM (1987) Deconvolution as a correction for photoelectron inelastic energy losses in the core level XPS spectra of iron oxides. Surf Interface Anal 10(2–3):63–74
89. Marcus P, Grimal J (1992) The anodic dissolution and passivation of NiCrFe alloys studied by ESCA. Corros Sci 33(5):805–814
90. Langevoort J, Sutherland I, Hanekamp L, Gellings P (1987) On the oxide formation on stainless steels AISI 304 and incoloy 800H investigated with XPS. Appl Surf Sci 28(2):167–179
91. Fujii T, De Groot F, Sawatzky G, Voogt F, Hibma T, Okada K (1999) In situ XPS analysis of various iron oxide films grown by NO 2-assisted molecular-beam epitaxy. Phys Rev B 59(4):3195
92. Petersson L, Karlsson S (1977) Clean and oxygen exposed potassium studied by photoelectron spectroscopy. Phys Scr 16(5–6):425
93. Sharma J, Gora T, Rimstidt J, Staley R (1972) X-ray photoelectron spectra of the alkali azides. Chem Phys Lett 15(2):232–235
94. Bard AJ, Faulkner LR (1980) Electrochemical Methods: Fundamentals and Applications, 2nd edn. Wiley, New York, U.S.A.
95. Alba-Molina D, Santiago ARP, Giner-Casares JJ, Rodríguez-Castellón E, Martín-Romero MT, Camacho L, Luque R, Cano M (2019) Tailoring the ORR and HER electrocatalytic performances of gold nanoparticles through metal–ligand interfaces. J Mater Chem A 7(35):20425–20434
96. Iwata R, Zhang L, Wilke KL, Gong S, He M, Gallant BM, Wang EN (2021) Bubble growth and departure modes on wettable/non-wettable porous foams in alkaline water splitting. Joule 5(4):887–900
97. Vickers JW, Alfonso D, Kauffman DR (2017) Electrochemical carbon dioxide reduction at nanostructured gold, copper, and alloy materials. Energy Technol 5(6):775–795
98. Mezzavilla S, Horch S, Stephens IE, Seger B, Chorkendorff I (2019) Structure sensitivity in the electrocatalytic reduction of CO2 with gold catalysts. Angew Chem Int Edit 58(12):3774–3778
99. Kas R, Yang K, Bohra D, Kortlever R, Burdyny T, Smith WA (2020) Electrochemical CO 2 reduction on nanostructured metal electrodes: fact or defect? Chem Sci 11(7):1738–1749
100. Koh JH, Jeon HS, Jee MS, Nursanto EB, Lee H, Hwang YJ, Min BK (2015) Oxygen plasma Induced hierarchically structured Gold Electrocatalyst for Selective reduction of Carbon Dioxide to Carbon Monoxide. J Phys Chem C 119(2):883–889. https://doi.org/10.1021/jp509967m
101. da Silva Freitas W, D'Epifanio A, Mecheri B (2021) Electrocatalytic CO2 reduction on nanostructured metal-based materials: Challenges and constraints for a sustainable pathway to decarbonization. J CO2 Utilization 50:101579. https://doi.org/10.1016/j.jcou.2021.101579
102. Suominen M, Kallio T (2021) What we currently know about Carbon-Supported metal and metal oxide nanomaterials in Electrochemical CO2 reduction. ChemElectroChem 8(13):2397–2406. https://doi.org/10.1002/celc.202100345
103. Gold Price in USA Today (2023) https://www.livepriceofgold.com/usa-gold-price.html. Accessed April 2,
104. Kreuer KD, Ise M, Fuchs A, Maier J (2000) Proton and water transport in nano-separated polymer membranes. J Phys IV France 10 (PR7):Pr7-279-Pr277-281
105. Sajjad SD, Gao Y, Liu Z, Yang H, Masel R (2017) Tunable-high performance Sustainion™ anion exchange membranes for electrochemical applications. ECS Trans 77(11):1653
106. Hori Y, Wakebe H, Tsukamoto T, Koga O (1994) Electrocatalytic process of CO selectivity in electrochemical reduction of CO2 at metal electrodes in aqueous media. Electrochim Acta 39(11–12):1833–1839. https://doi.org/10.1016/0013-4686(94)85172-7
107. Hori Y (2008) Electrochemical CO 2 reduction on metal electrodes. Modern aspects of electrochemistry:89–189
108. Costentin C, Robert M, Savéant J-M (2013) Catalysis of the Electrochemical reduction of Carbon Dioxide. Chem Soc Rev 42(6):2423–2436
109. Shi S, Weber AZ, Kusoglu A (2016) Structure-transport relationship of perfluorosulfonic-acid membranes in different cationic forms. Electrochim Acta 220:517–528
110. Webb T (1926) The free energy of hydration of ions and the electrostriction of the solvent. J Am Chem Soc 48(10):2589–2603
111. Flett D, Meares P (1966) Thermodynamics of cation exchange. Part 4.—Uni-, bi-and tervalent ions on Dowex 50. T Faraday Soc 62:1469–1481
112. Steck A, Yeager H (1980) Water sorption and cation-exchange selectivity of a perfluorosulfonate ion-exchange polymer. Anal Chem 52(8):1215–1218
113. Resasco J, Chen LD, Clark E, Tsai C, Hahn C, Jaramillo TF, Chan K, Bell AT (2017) Promoter effects of alkali metal cations on the electrochemical reduction of carbon dioxide. J Am Chem Soc 139(32):11277–11287
114. Ringe S, Clark EL, Resasco J, Walton A, Seger B, Bell AT, Chan K (2019) Understanding cation effects in electrochemical CO 2 reduction. Energy Environ Sci 12(10):3001–3014
115. Ringe S, Morales-Guio CG, Chen LD, Fields M, Jaramillo TF, Hahn C, Chan K (2020) Double layer charging driven carbon dioxide adsorption limits the rate of electrochemical carbon dioxide reduction on gold. Nat Commun 11(1):33
116. Zhu Q, Wallentine SK, Deng G-H, Rebstock JA, Baker LR (2022) The Solvation-Induced Onsager reaction field rather than the double-layer field controls CO2 reduction on gold. JACS Au 2(2):472–482. https://doi.org/10.1021/jacsau.1c00512
117. Zhu Q, Murphy CJ, Baker LR (2022) Opportunities for Electrocatalytic CO2 reduction enabled by Surface Ligands. J Am Chem Soc 144(7):2829–2840. https://doi.org/10.1021/jacs.1c11500
118. Marcandalli G, Boterman K, Koper MTM (2022) Understanding hydrogen evolution reaction in bicarbonate buffer. J Catal 405:346–354. https://doi.org/10.1016/j.jcat.2021.12.012
119. Kusoglu A, Weber AZ (2017) New insights into perfluorinated sulfonic-acid ionomers. Chem Rev 117(3):987–1104
120. Ren X, Myles TD, Grew KN, Chiu WK (2015) Carbon dioxide transport in Nafion 1100 EW membrane and in a direct methanol fuel cell. J Electrochem Soc 162(10):F1221
121. Okada T, Satou H, Okuno M, Yuasa M (2002) Ion and water transport characteristics of perfluorosulfonated ionomer membranes with H + and alkali metal cations. J Phys Chem B 106(6):1267–1273
122. Dunwell M, Lu Q, Heyes JM, Rosen J, Chen JG, Yan Y, Jiao F, Xu B (2017) The central role of bicarbonate in the electrochemical reduction of carbon dioxide on gold. J Am Chem Soc 139(10):3774–3783
123. Calvinho KU, Laursen AB, Yap KM, Goetjen TA, Hwang S, Murali N, Mejia-Sosa B, Lubarski A, Teeluck KM, Hall ES (2018) Selective CO 2 reduction to C 3 and C 4 oxyhydrocarbons on nickel phosphides at overpotentials as low as 10 mV. Energy Environ Sci 11(9):2550–2559